

A stochastic kinetic scheme for multi-scale plasma transport with uncertainty quantification



Tianbai Xiao*, Martin Frank

Karlsruhe Institute of Technology, Karlsruhe, Germany

ARTICLE INFO

Article history:

Available online 23 January 2021

Keywords:

Boltzmann equation
Plasma physics
Kinetic theory
Uncertainty quantification
Multi-scale methods

ABSTRACT

Plasmas present a diverse set of behaviors in different regimes. Given the intrinsic multi-scale nature of plasma dynamics, classical theoretical and numerical methods are often employed at separate scales with corresponding assumptions and approximations. Clearly, the coarse-grained modeling may introduce considerable uncertainties between the field solutions of flow and electromagnetic variables, and the real plasma physics. To study the emergence, propagation and evolution of randomness from gyrations of charged particles to magnetohydrodynamics poses great opportunities and challenges to develop both sound theories and reliable numerical algorithms. In this paper, a physics-oriented stochastic kinetic scheme will be developed that includes random inputs from both flow and electromagnetic fields via a hybridization of stochastic Galerkin and collocation methods. Based on the BGK-type relaxation model of the multi-component Boltzmann equation, a scale-dependent kinetic central-upwind flux function is designed in both physical and particle velocity space, and the governing equations in the discrete temporal-spatial-random domain are constructed. By solving Maxwell's equations with the wave-propagation method, the evolutions of ions, electrons and electromagnetic field are coupled throughout the simulation. We prove that the scheme is formally asymptotic-preserving in the Vlasov, magnetohydrodynamical, and neutral Euler regimes with the inclusion of random variables. Therefore, it can be used for the study of multi-scale and multi-physics plasma system under the effects of uncertainties, and provide scale-adaptive physical solutions under different ratios among numerical cell size, particle mean free path and gyroradius (or time step, local particle collision time and plasma period). Numerical experiments including one-dimensional Landau Damping, the two-stream instability and the Brio-Wu shock tube problem with one- to three-dimensional velocity settings, and each under stochastic initial conditions with one-dimensional uncertainty, will be presented to validate the scheme.

© 2021 Elsevier Inc. All rights reserved.

1. Introduction

Plasma applications can cover an extremely wide range of particle number density and temperature. As F. Chen wrote in his famous monograph [1], "What makes plasmas particularly difficult to analyze is the fact that the densities fall in an intermediate range. They behave sometimes like fluids, and sometimes like a collection of individual particles." A qualitative

* Corresponding author.

E-mail addresses: tianbaixiao@gmail.com (T. Xiao), martin.frank@kit.edu (M. Frank).

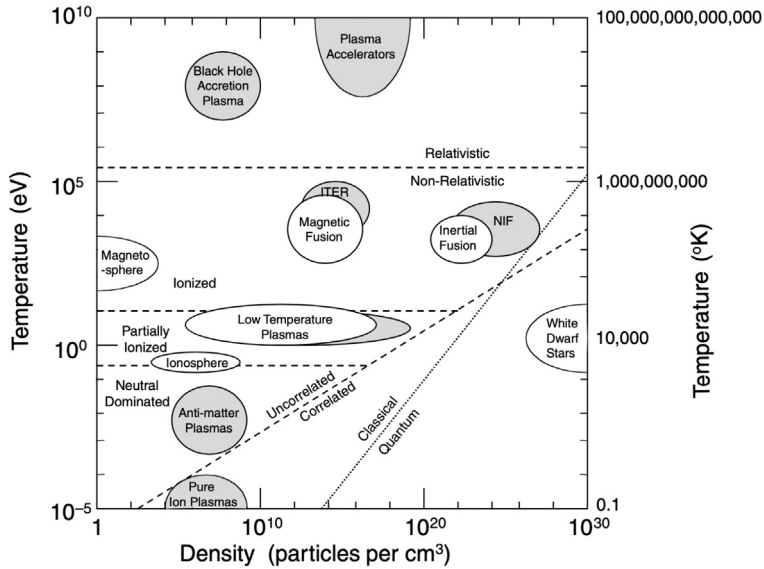


Fig. 1. An illustrative demonstration of different plasma regimes and related phenomena [2].

classification of typical plasma regimes with respect to density and temperature is presented in Fig. 1. In this paper, we confine ourselves to the study of classical, non-relativistic and weakly coupled plasmas, e.g. the magnetosphere, whose behaviors can be well described by the kinetic theory of gases.

Given the intrinsic multi-scale nature in plasma physics, classical theories are devoted to different governing equations at different hierarchies. For example, at a particle mean free path which is larger than the Debye length $\lambda_D = (\epsilon_0 k_B T_{ele}/ne^2)^{1/2}$, and a mean collision time which is larger than the reciprocal of the plasma frequency $\omega_p = (ne^2/\epsilon_0 m_{ion})^{1/2}$, the motions of ions and electrons can be depicted statistically through kinetic equations, e.g. the Vlasov equation and the Fokker-Planck-Landau equation. On the other hand, at the macroscopic level with intensive intermolecular collisions, the fluid dynamic equations are routinely used to model the collective behaviors of charged particles, i.e. the magnetohydrodynamics (MHD) equations.

Since the 1950s, rapid development has been made in deterministic numerical methods for plasma simulations [3–10]. However, given the coarse-grained approximation in the field theories of plasmas and errors inherited from numerical simulations, considerable uncertainties may be introduced inevitably. One typical example are the uncertain inputs of the initial/boundary value problem. Furthermore, for the evaluation of collision kernel in the kinetic equations, the phenomenological model parameters often need to be calibrated by experiments to reproduce correct transport coefficients, which introduce errors into the simulations [11]. Another example goes to the vacuum permeability employed in the Maxwell's equations for electromagnetic fields. In the SI system which has gone into force in 2019 [12], this value is measured experimentally as $\mu_0 = 8.8541878128 \times 10^{-12} \text{ F}\cdot\text{m}^{-1}$, with a relative standard deviation being 1.5×10^{-10} .

Uncertainty quantification (UQ) is a thriving subject that quantifies one's lack of knowledge concerning a physical reality. It applies itself to answer the challenging questions, e.g. how predictive are the simulation results from the idealized models, and how can one explicitly assess the effects of uncertainties on the quality of model predictions. Depending on the methodology to model the random variables, the methods for UQ study can be classified into intrusive and non-intrusive ones. In the former case, a series of realizations of random inputs are generated based on a prescribed probability distribution. Each realization is solved by a deterministic solver, and then a post-processing is employed to estimate the uncertainties. In contrast, intrusive methods work in a way such that we reformulate the original deterministic system.

One prevalent intrusive strategy is the stochastic Galerkin (SG) method [13], in which the solutions are expressed into orthogonal polynomials of the input random parameters. It promises spectral convergence in random space when the solution depends smoothly on the stochastic parameters [14]. In a nonlinear Galerkin system, all the expansion coefficients are essentially coupled, which becomes cumbersome in massive computations. The stochastic collocation (SC) method [15], although a non-intrusive method, can be seen as a middle way. It combines the strengths of non-intrusive sampling and SG by evaluating the generalized polynomial chaos (gPC) expansions on quadrature points in random space. As a result, a set of decoupled equations can be derived and solved with deterministic solvers on each quadrature point. Provided the solutions possess sufficient smoothness over random space, the SC methods maintain similar convergence as SG, but suffers from aliasing errors due to limited number of quadrature points.

Although the UQ field has undergone rapid development over the past few years, its applications on plasma physics mainly focus on the two limits of Vlasov [16–18] and MHD [19,20] with standard stochastic settings. With the work in fluid dynamics [21,22], to the best of the authors' knowledge, limited work has been conducted on the evolutionary process of uncertainty in multi-scale plasma physics. Given the nonlinear system including intermolecular collisions, initial

inputs, fluid-surface interactions and geometric complexities, uncertainties may emerge from molecular-level nature, develop upwards, affect macroscopic collective behaviors, and vice versa. To study the emergence, propagation and evolution of uncertainty poses great opportunities and challenges to develop both sound theories and reliable multi-scale numerical algorithms.

It is noticeable that tracking the evolution of stochastic variables with either polynomial chaos or quadrature rules is similar in spirit to solving kinetic equations in phase space with moment or discrete velocity methods. The advantages of SG and SC methods can be combined when the integrals that are necessary for SG inside the algorithm are computed numerically using SC. In this paper, we follow the strategy proposed in [23] and develop a stochastic kinetic scheme for multi-scale plasma transport and we couple it to Maxwell's equations. Based on the Bhatnagar-Gross-Krook (BGK) type relaxation model for multi-component plasmas, a scale-dependent central-upwind flux is constructed spanning physical, velocity and random space. We follow the strategy that has been applied in the unified gas-kinetic scheme for deterministic solutions [36,37], and present a natural extension in the stochastic context. The update of source terms of plasma and electromagnetic fields are solved in a coupled way implicitly. We thus combine the advantages of SG and SC methods with the construction principle of kinetic schemes, and obtain an efficient and accurate scheme for cross-scale BGK-Maxwell system with uncertainties. The randomly initial inputs of both flow and electromagnetic fields are considered.

The rest of this paper is organized as follows. Sec. 2 is a brief introduction of kinetic theory of plasma and its stochastic formulation. Sec. 3 presents the numerical implementation of the current scheme and detailed solution algorithm. Sec. 4 includes numerical experiments to demonstrate the performance of the current scheme and analyze some new physical observations. The last section is the conclusion.

2. Deterministic and stochastic theories

2.1. Kinetic theory of plasmas

The gas kinetic theory describes the time-space evolution of particle distribution function. With a separate modeling of particle transport and collision processes, the evolution equation of monatomic plasmas writes as

$$\frac{\partial f_\alpha}{\partial t} + \mathbf{u} \cdot \nabla_{\mathbf{x}} f_\alpha + \frac{q_\alpha}{m_\alpha} (\mathbf{E} + \mathbf{u} \times \mathbf{B}) \cdot \nabla_{\mathbf{u}} f_\alpha = Q_\alpha, \quad (1)$$

where $\alpha = \text{ion, ele}$ denotes a specific ion or electron, (q_α, m_α) are particle charge and mass, and (\mathbf{E}, \mathbf{B}) are electric and magnetic fields respectively. $Q(f)$ is the multi-component Boltzmann collision integral. For the Coulomb collisions between charged particles, the limiting case of Boltzmann collision integral with small scattering angles leads to the Fokker-Planck-Landau operator,

$$Q_\alpha = \sum_{\beta}^N \left\{ \nabla_{\mathbf{u}} \cdot \int \Phi(\mathbf{u} - \mathbf{u}') [f_\beta(\mathbf{u}') \nabla_{\mathbf{u}} f_\alpha(\mathbf{u}) - f_\alpha(\mathbf{u}) \nabla_{\mathbf{u}} f_\beta(\mathbf{u}')] d\mathbf{u}' \right\}, \quad (2)$$

where $(\mathbf{u}, \mathbf{u}')$ are the velocities of two classes of particles and $\Phi(\mathbf{u}) = (|\mathbf{u}|^2 \mathbf{I}_3 - \mathbf{u} \otimes \mathbf{u}) / |\mathbf{u}|^3$ is a 3×3 matrix.

Solving the convolution-type collision operator is time consuming. Let us take an example of the spectral algorithm based on the fast Fourier transformation [24], which is one of the most efficient numerical methods by far. The computational cost of it for pure matter is of $O(M^2 N^3 \log N)$, where N is the number of quadrature points in each velocity direction and M^2 is the number of discrete solid angles. When the method is extended to multi-component particles, as analyzed in [25,26], the computational cost increases to $O(m_r^{0.5} M^2 N^4 \log N)$, where m_r is the mass ratio of the heavier to lighter species. In plasma applications, m_r is extremely large, resulting in significant increase of the computational cost. Also, for the study of uncertainty quantification, an additional probabilistic space needs to be introduced. The variables are coupled with respect to the randomness, which again increases the computational cost in a nonlinear way. Therefore, it's unwise to employ full Fokker-Planck-Landau model, if not impossible.

Instead of solving the above collision integral directly, here we employ a multi-component BGK-type relaxation model proposed by Andries, Aoki and Perthame [27] in the current work to mimic the collision process,

$$Q_\alpha = \nu_\alpha (\mathcal{M}_\alpha - f_\alpha), \quad (3)$$

where ν_α is the collision frequency. The equilibrium distribution is defined based on the local modified macroscopic variables, i.e.,

$$\mathcal{M}_\alpha = n_\alpha \left(\frac{m_\alpha}{2\pi k_B \bar{T}_\alpha} \right)^{\frac{3}{2}} \exp \left(-\frac{m_\alpha}{2k_B \bar{T}_\alpha} (\mathbf{u} - \bar{\mathbf{U}}_\alpha)^2 \right), \quad (4)$$

where n_α is number density, m_α is molecular mass and k_B is the Boltzmann constant. The design of modified temperature \bar{T}_α and velocity $\bar{\mathbf{U}}_\alpha$ is based on the idea that the macroscopic transfer rates in the moments equations derived from BGK

model should be consistent with that from multi-component Boltzmann equation. For elastic scattering, the evaluation of modified variables for Maxwell and hard sphere molecules can be written as,

$$\begin{aligned}\bar{\mathbf{U}}_\alpha &= \mathbf{U}_\alpha + \tau_\alpha \sum_r \frac{2m_r}{m_\alpha + m_r} v_{\alpha r} (\mathbf{U}_r - \mathbf{U}_\alpha), \\ \frac{3}{2} k_B \bar{T}_\alpha &= \frac{3}{2} k_B T_\alpha - \frac{m_\alpha}{2} (\bar{\mathbf{U}}_\alpha - \mathbf{U}_\alpha)^2 \\ &+ \tau_\alpha \sum_r \frac{4m_\alpha m_r}{(m_\alpha + m_r)^2} v_{\alpha r} \left[\frac{3}{2} k_B T_r - \frac{3}{2} k_B T_\alpha + \frac{m_r}{2} (\mathbf{U}_r - \mathbf{U}_\alpha)^2 \right],\end{aligned}\quad (5)$$

where $v_{\alpha r}$ is the frequency of intermolecular interactions which can be derived through specific molecule models [28], and it determines the relaxation time by $\tau_\alpha = 1 / \sum_r^N v_{\alpha r}$. For example, for the hard-sphere molecules, the interaction frequency is defined as,

$$v_{\alpha r} = \frac{4\sqrt{\pi} n_r}{3} \left(\frac{2k_B T_\alpha}{m_\alpha} + \frac{2k_B T_r}{m_r} \right)^{1/2} \left(\frac{d_\alpha + d_r}{2} \right)^2, \quad (6)$$

where d is the kinetic molecule diameter. As analyzed [27], the relaxation model satisfies key properties, i.e. positivity, correct exchange coefficients, entropy inequality, and indifferentiability principle. Designed for the Maxwell molecules, it is under similar restriction of unit Prandtl number as the original BGK model when extended to more general molecule models. Similar correction techniques, e.g. the Shakhov, can be conducted correspondingly [29].

Macroscopic conservative flow variables are related to the moments of the particle distribution function,

$$\mathbf{W}_\alpha = \begin{pmatrix} \rho_\alpha \\ \rho_\alpha \mathbf{U}_\alpha \\ \rho_\alpha \mathcal{E}_\alpha \end{pmatrix} = \int m_\alpha f_\alpha \varpi d\mathbf{u}, \quad (7)$$

where $\mathcal{E}_\alpha = (\mathbf{U}_\alpha)^2 / 2 + 3k_B T_\alpha / 2m_\alpha$ is total energy density, and $\varpi = (1, \mathbf{u}, \frac{1}{2}\mathbf{u}^2)^T$ is the vector of collision invariants. Hence, macroscopic transport equations can be derived by taking moments of the kinetic equation with respect to the collision invariants, i.e.,

$$\begin{aligned}\frac{\partial n_\alpha}{\partial t} + \nabla_{\mathbf{x}} \cdot (n_\alpha \mathbf{U}_\alpha) &= 0, \\ \frac{\partial(\rho_\alpha \mathbf{U}_\alpha)}{\partial t} + \nabla_{\mathbf{x}} \cdot (\rho_\alpha \mathbf{U}_\alpha \mathbf{U}_\alpha) &= \nabla_{\mathbf{x}} \cdot \mathbf{P}_\alpha + n_\alpha q_\alpha (\mathbf{E} + \mathbf{U}_\alpha \times \mathbf{B}) + \mathbf{R}_\alpha, \\ \frac{\partial(\rho_\alpha \mathcal{E}_\alpha)}{\partial t} + \nabla_{\mathbf{x}} \cdot (\rho_\alpha \mathcal{E}_\alpha \mathbf{U}_\alpha) &= \nabla_{\mathbf{x}} \cdot (\mathbf{P}_\alpha \mathbf{U}_\alpha) - \nabla_{\mathbf{x}} \cdot \mathbf{q}_\alpha + n_\alpha q_\alpha \mathbf{U}_\alpha \cdot \mathbf{E} + H_\alpha,\end{aligned}\quad (8)$$

where the source terms \mathbf{R}_α and H_α in the balance laws come from the moments of collision term respectively,

$$\begin{aligned}\mathbf{R}_\alpha &= \int \mathbf{u} m_\alpha v_\alpha (\mathcal{M}_\alpha - f_\alpha) d\mathbf{u} = \sum_r \frac{2m_r m_r}{m_\alpha + m_r} n_\alpha v_{\alpha r} (\mathbf{U}_r - \mathbf{U}_\alpha), \\ H_\alpha &= \int \frac{1}{2} (\mathbf{u} - \mathbf{U})^2 m_\alpha v_\alpha (\mathcal{M}_\alpha - f_\alpha) d\mathbf{u} \\ &= \sum_r \frac{4m_\alpha m_r}{(m_\alpha + m_r)^2} n_\alpha v_{\alpha r} \left[\frac{3}{2} k_B T_r - \frac{3}{2} k_B T_\alpha + \frac{m_r}{2} (\mathbf{U}_r - \mathbf{U}_\alpha)^2 \right].\end{aligned}\quad (9)$$

Eq. (8) is consistent with the well-known Braginskii's two-fluid model [30]. The current BGK model provides credible physical mechanism in both collisionless and hydrodynamic limits. In the upper transition regime, it might be less accurate than the Fokker-Planck-Landau model due to the tidier degrees of freedom. Therefore, the current work is not to recover the exact Fokker-Planck solutions in all regimes, but to employ discrete velocity settings to construct a multi-scale two-fluid model, where the particle distribution functions enjoy space-time evolution instead of taking fixed forms from closure ansatz, and to study the stochastic evolution of plasmas in the context of uncertainty quantification.

2.2. Generalized polynomial chaos approximation of kinetic equation with uncertainties

Several sources of uncertainty can be considered in the BGK equation. Here we consider uncertain initial and boundary conditions, which turn the deterministic system into stochastic case. We employ the generalized polynomial chaos (gPC) expansion of particle distribution with degree N , i.e.,

$$f_\alpha(t, \mathbf{x}, \mathbf{u}, \mathbf{z}) \simeq f_{\alpha N} = \sum_{|i|=0}^N \hat{f}_{\alpha i}(t, \mathbf{x}, \mathbf{u}) \Phi_i(\mathbf{z}) = \hat{\mathbf{f}}_\alpha^T \Phi, \quad (10)$$

where i could be a scalar or a K -dimensional vector $i = (i_1, i_2, \dots, i_K)$ with $|i| = i_1 + i_2 + \dots + i_K$. The $\hat{f}_{\alpha i}$ is the coefficient of i -th polynomial chaos expansion, and the basis functions used are orthogonal polynomials $\{\Phi_i(\mathbf{z})\}$ satisfying the following constraints,

$$\mathbb{E}[\Phi_j(\mathbf{z})\Phi_k(\mathbf{z})] = \gamma_k \delta_{jk}, \quad 0 \leq |j|, |k| \leq N, \quad (11)$$

where

$$\gamma_k = \mathbb{E}[\Phi_k^2(\mathbf{z})], \quad 0 \leq |k| \leq N, \quad (12)$$

are the normalization factors. The expectation value defines a scalar product,

$$\mathbb{E}[\Phi_j(\mathbf{z})\Phi_k(\mathbf{z})] = \int_{\mathbf{z}} \Phi_j(\mathbf{z})\Phi_k(\mathbf{z})\varrho(\mathbf{z})d\mathbf{z}, \quad (13)$$

where $\varrho(\mathbf{z})$ is the probability density function. In practice, it can be evaluated theoretically or with numerical quadrature rule, i.e.,

$$\mathbb{E}[\Phi_j(\mathbf{z})\Phi_k(\mathbf{z})] = \sum_i \Phi_j(\mathbf{z}_i)\Phi_k(\mathbf{z}_i)w(\mathbf{z}_i), \quad (14)$$

where $w(\mathbf{z}_i)$ is the corresponding quadrature weight function in random space. In the following we adopt a uniform notation $\langle \Phi_j \Phi_k \rangle$ to denote the integrals over random space from Eq. (13) and (14).

Given the correspondence between macroscopic and mesoscopic variables, from Eq. (7) we can derive,

$$\begin{aligned} \mathbf{W}_\alpha &\simeq \int f_{\alpha N} \varpi d\mathbf{u} = \int \sum_{|i|=0}^N \hat{f}_{\alpha i}(t, \mathbf{x}, \mathbf{u}) \Phi_i(\mathbf{z}) \varpi d\mathbf{u} = \sum_{|i|=0}^N \left(\int \hat{f}_{\alpha i} \varpi d\mathbf{u} \right) \Phi_i \\ &\simeq \mathbf{W}_{\alpha N} = \sum_{|i|=0}^N \hat{w}_{\alpha i} \Phi_i = \hat{\mathbf{w}}_\alpha^T \Phi. \end{aligned} \quad (15)$$

After substituting the Eq. (10) into the kinetic equation (1) and (3), and performing a Galerkin projection, we then obtain

$$\frac{\partial \hat{\mathbf{f}}_\alpha}{\partial t} + \mathbf{u} \cdot \nabla_{\mathbf{x}} \hat{\mathbf{f}}_\alpha + \hat{\mathbf{G}}_\alpha = \hat{\mathbf{Q}}_\alpha = v_\alpha (\hat{\mathbf{m}}_\alpha - \hat{\mathbf{f}}_\alpha), \quad (16)$$

where $\hat{\mathbf{Q}}_\alpha$ is the gPC coefficient vector of the projection from collision operator to the polynomial basis,

$$\hat{\mathbf{Q}}_\alpha = v_\alpha (\hat{\mathbf{m}}_\alpha - \hat{\mathbf{f}}_\alpha), \quad (17)$$

with $\hat{\mathbf{m}}_\alpha$ being the vector of gPC coefficients of Maxwellian distribution (which depends implicitly on the $\hat{\mathbf{f}}_\alpha$) and v_α being a deterministic collision frequency. The electromagnetic forcing term $\hat{\mathbf{G}}_\alpha$ is

$$\hat{\mathbf{G}}_\alpha = \hat{\mathbf{G}}_\alpha^T \Phi = \sum_{|i|=0}^N \hat{G}_i \Phi_i, \quad \hat{G}_i = \frac{q_\alpha}{m_\alpha} \frac{\sum_j^N \sum_k^N (\hat{\mathbf{E}}_j + \mathbf{u} \times \hat{\mathbf{B}}_j) \nabla_{\mathbf{u}} \hat{f}_{\alpha k} \langle \Phi_j \Phi_k \Phi_i \rangle}{\langle \Phi_i^2 \rangle}. \quad (18)$$

Notice that the gPC coefficients of both $\hat{\mathbf{G}}_\alpha$ and $\hat{\mathbf{Q}}_\alpha$ are nonlinear functions of the state variables (cf. Eq. (5)).

2.3. Maxwellian distribution in generalized polynomial chaos

For a deterministic system, the evaluation of the Maxwellian distribution given in Eq. (4) is straight-forward. However, given a generalized polynomial chaos (gPC) system, the multiplication and division can't be operated directly on the stochastic moments without modifying the orthogonal basis. Starting from a known particle distribution function in Eq. (10), here we draw a brief outline to approximately evaluate the Maxwellian distribution function in the gPC expansion.

1. Derive the macroscopic conservative variables from particle distribution function with gPC expansion,

$$\mathbf{W}_{\alpha N} = \begin{pmatrix} \rho_{\alpha N} \\ (\rho_\alpha \mathbf{U}_\alpha)_N \\ (\rho_\alpha \mathcal{E}_\alpha)_N \end{pmatrix} = \sum_{|i|=0}^N \left(\int \hat{f}_{\alpha i} \psi d\mathbf{u} \right) \Phi_i; \quad (19)$$

2. Locate conservative variables on quadrature points \mathbf{z}_j of random space and calculate primitive variables, e.g. flow velocity

$$\mathbf{U}_\alpha(\mathbf{z}_j) = \frac{(\rho_\alpha \mathbf{U}_\alpha)_N(\mathbf{z}_j)}{\rho_{\alpha N}(\mathbf{z}_j)}, \quad (20)$$

and

$$T_\alpha(\mathbf{z}_j) = \frac{(\rho_\alpha E_\alpha)_N(\mathbf{z}_j) - (\rho_\alpha U_\alpha)_N^2(\mathbf{z}_j)/2\rho_{\alpha N}(\mathbf{z}_j)}{3k_B \rho_{\alpha N}/2m_\alpha}, \quad (21)$$

and then calculate the modified velocity and temperature via Eq. (5).

3. Calculate Maxwellian distribution on quadrature points

$$\mathcal{M}_\alpha(\mathbf{z}_j) = n_\alpha(\mathbf{z}_j) \left(\frac{m_\alpha}{2\pi k_B \bar{T}_\alpha(\mathbf{z}_j)} \right)^{\frac{3}{2}} e^{-\bar{\lambda}_\alpha(\mathbf{z}_j)(\mathbf{u} - \bar{\mathbf{U}}_\alpha(\mathbf{z}_j))^2}, \quad (22)$$

and decompose it into a gPC expansion

$$\mathcal{M}_{\alpha N} = \sum_{|\mathbf{i}|=0}^N \hat{m}_{\alpha i} \Phi_i, \quad (23)$$

with each coefficient in the expansion being given by a quadrature rule

$$\hat{m}_{\alpha i} = \frac{\langle \mathcal{M}_\alpha, \Phi_i \rangle}{\langle \Phi_i^2 \rangle} = \frac{\sum_j \mathcal{M}_\alpha(\mathbf{z}_j) \Phi_i(\mathbf{z}_j) Q(\mathbf{z}_j)}{\int_{I_z} (\Phi_i(\mathbf{z}))^2 Q(\mathbf{z}) d\mathbf{z}}. \quad (24)$$

2.4. Maxwell's equations

For the self-consistent problem of plasma dynamics, the evolutions of electric and magnetic fields (\mathbf{E}, \mathbf{B}) are coupled with the motions of charged particles, which can be described by the linear Maxwell's equations in vacuum,

$$\begin{aligned} \frac{\partial \mathbf{E}}{\partial t} - c^2 \nabla_{\mathbf{x}} \times \mathbf{B} &= -\frac{1}{\epsilon_0} \mathbf{J}, \\ \frac{\partial \mathbf{B}}{\partial t} + \nabla_{\mathbf{x}} \times \mathbf{E} &= 0, \\ \nabla_{\mathbf{x}} \cdot \mathbf{E} &= \frac{\sigma}{\epsilon_0}, \\ \nabla_{\mathbf{x}} \cdot \mathbf{B} &= 0. \end{aligned} \quad (25)$$

Here $\sigma = e(n_i - n_e)$ is the net charge density, \mathbf{J} is the current, and the speed of light is related to the permeability and permittivity of vacuum with $c = (\mu_0 \epsilon_0)^{-1/2}$. To ensure the divergence constraints in numerical simulations, some techniques can be used in solving Maxwell's equations. Here we employ the perfectly hyperbolic Maxwell's equations (PHM) [31],

$$\begin{aligned} \frac{\partial \mathbf{E}}{\partial t} - c^2 \nabla_{\mathbf{x}} \times \mathbf{B} + \chi c^2 \nabla_{\mathbf{x}} \phi &= -\frac{1}{\epsilon_0} \mathbf{J}, \\ \frac{\partial \mathbf{B}}{\partial t} + \nabla_{\mathbf{x}} \times \mathbf{E} + \gamma \nabla_{\mathbf{x}} \psi &= 0, \\ \frac{1}{\chi} \frac{\partial \phi}{\partial t} + \nabla_{\mathbf{x}} \cdot \mathbf{E} &= \frac{\sigma}{\epsilon_0}, \\ \frac{\epsilon_0 \mu_0}{\gamma} \frac{\partial \psi}{\partial t} + \nabla_{\mathbf{x}} \cdot \mathbf{B} &= 0, \end{aligned} \quad (26)$$

where ϕ, ψ are two additional correction potentials, and the propagation speed of errors for the divergence of magnetic and electric fields are γc and χc correspondingly. With the stochastic Galerkin formulation, the PHM system can be rewritten as

$$\begin{aligned}
\frac{\partial \hat{\mathbf{E}}}{\partial t} - c^2 \nabla_{\mathbf{x}} \times \hat{\mathbf{B}} + \chi c^2 \nabla_{\mathbf{x}} \hat{\phi} &= -(\mathbf{J}/\varepsilon_0), \\
\frac{\partial \hat{\mathbf{B}}}{\partial t} + \nabla_{\mathbf{x}} \times \hat{\mathbf{E}} + \gamma \nabla_{\mathbf{x}} \hat{\psi} &= 0, \\
\frac{1}{\chi} \frac{\partial \hat{\phi}}{\partial t} + \nabla_{\mathbf{x}} \cdot \hat{\mathbf{E}} &= (\sigma/\varepsilon_0), \\
\frac{\varepsilon_0 \mu_0}{\gamma} \frac{\partial \hat{\psi}}{\partial t} + \nabla_{\mathbf{x}} \cdot \hat{\mathbf{B}} &= 0.
\end{aligned} \tag{27}$$

The parameters in Maxwell's equations are assumed to be deterministic. Notice the permittivity ε_0 can be uncertain, and thus the right-hand side of the above equations denotes the gPC coefficients of divisors.

3. Solution algorithm

3.1. Update algorithm

The current numerical algorithm is implemented within the finite volume framework. We adopt the notation of cell averaged macroscopic conservative variables and particle distribution function in a control volume,

$$\begin{aligned}
\mathbf{W}_\alpha(t^n, \mathbf{x}_i, \mathbf{z}_k) &= (\mathbf{W}_\alpha)_{i,k}^n = \frac{1}{\Omega_i(\mathbf{x})\Omega_k(\mathbf{z})} \int_{\Omega_i} \int_{\Omega_k} \mathbf{W}_\alpha(t^n, \mathbf{x}, \mathbf{z}) d\mathbf{x} d\mathbf{z}, \\
f_\alpha(t^n, \mathbf{x}_i, \mathbf{u}_j, \mathbf{z}_k) &= (f_\alpha)_{i,j,k}^n = \frac{1}{\Omega_i(\mathbf{x})\Omega_j(\mathbf{u})\Omega_k(\mathbf{z})} \int_{\Omega_i} \int_{\Omega_j} \int_{\Omega_k} f_\alpha(t^n, \mathbf{x}, \mathbf{u}, \mathbf{z}) d\mathbf{x} d\mathbf{u} d\mathbf{z},
\end{aligned}$$

along with the coefficient vector in the gPC expansions,

$$\begin{aligned}
\hat{\mathbf{W}}_\alpha(t^n, \mathbf{x}_i) &= (\hat{\mathbf{W}}_\alpha)_i^n = \frac{1}{\Omega_i(\mathbf{x})} \int_{\Omega_i} \hat{\mathbf{W}}_\alpha(t^n, \mathbf{x}) d\mathbf{x}, \\
\hat{\mathbf{f}}_\alpha(t^n, \mathbf{x}_i, \mathbf{u}_j) &= (\hat{\mathbf{f}}_\alpha)_{i,j}^n = \frac{1}{\Omega_i(\mathbf{x})\Omega_j(\mathbf{u})} \int_{\Omega_i} \int_{\Omega_j} \hat{\mathbf{f}}_\alpha(t^n, \mathbf{x}, \mathbf{u}) d\mathbf{x} d\mathbf{u},
\end{aligned}$$

where Ω_i , Ω_j and Ω_k are the cell area in the discretized physical, velocity and random space.

The update of the stochastic Galerkin coefficients for particle distribution function can be written as,

$$\begin{aligned}
(\hat{\mathbf{f}}_\alpha)_{i,j}^{n+1} &= (\hat{\mathbf{f}}_\alpha)_{i,j}^n + \frac{1}{\Omega_i} \int_{t^n}^{t^{n+1}} \sum_{S_r \in \partial \Omega_i} S_r (\hat{\mathbf{F}}_\alpha)_{r,j}^f dt \\
&\quad + \frac{1}{\Omega_j} \int_{t^n}^{t^{n+1}} \sum_{S_r \in \partial \Omega_j} S_r (\hat{\mathbf{F}}_\alpha)_{i,r}^f dt + \int_{t^n}^{t^{n+1}} (\hat{\mathbf{Q}}_\alpha)_{i,j}^f dt,
\end{aligned} \tag{28}$$

where $(\hat{\mathbf{F}}_\alpha)_r^f$ is the time-dependent fluxes for distribution function at interface r in physical and velocity space, S_r is the interface area, and $\hat{\mathbf{Q}}_\alpha^f$ is the collision term. Taking velocity moments of Eq. (28), we obtain the corresponding macroscopic system,

$$\begin{aligned}
(\hat{\mathbf{W}}_\alpha)_i^{n+1} &= (\hat{\mathbf{W}}_\alpha)_i^n + \frac{1}{\Omega_i} \int_{t^n}^{t^{n+1}} \sum_{S_r \in \partial \Omega_i} \mathbf{S}_r \cdot (\hat{\mathbf{F}}_\alpha)_r^W dt \\
&\quad + \int_{t^n}^{t^{n+1}} (\hat{\mathbf{G}}_\alpha)_i^W dt + \int_{t^n}^{t^{n+1}} (\hat{\mathbf{Q}}_\alpha)_i^W dt,
\end{aligned} \tag{29}$$

where $(\hat{\mathbf{F}}_\alpha)_r^W$ is the flux functions for macroscopic conservative variables, $\mathbf{S}_r = \mathbf{n} S_r$ is the interface area vector, and $\hat{\mathbf{G}}_\alpha^W$ is the external force terms related to Eq. (8).

Notice that the gPC coefficients of different orders are coupled through the external force term $\hat{\mathbf{G}}_\alpha$ (17) and the collision term $\hat{\mathbf{Q}}_\alpha$ (18). Instead of solving this large nonlinear system, we can locate the gPC system onto the collocation points in random space. It results a decoupled system that can be solved efficiently. Therefore, we combine the advantages of stochastic Galerkin and collocation methods, which is one of the novelties of this paper. To make use of it, in the solution algorithm, we first update the gPC coefficients to an intermediate step t^* ,

$$\begin{aligned} (\hat{\mathbf{W}}_\alpha)_i^* &= (\hat{\mathbf{W}}_\alpha)_i^n + \frac{1}{\Omega_i} \int_{t^n}^{t^{n+1}} \sum_{S_r \in \partial\Omega_i} \mathbf{S}_r \cdot (\hat{\mathbf{F}}_\alpha)_r^W dt, \\ (\hat{\mathbf{f}}_\alpha)_{i,j}^* &= (\hat{\mathbf{f}}_\alpha)_{i,j}^n + \frac{1}{\Omega_i} \int_{t^n}^{t^{n+1}} \sum_{S_r \in \partial\Omega_i} S_r (\hat{\mathbf{F}}_\alpha)_{r,j}^f dt, \end{aligned} \quad (30)$$

which are then evaluated on random quadrature cell Ω_k ,

$$\begin{aligned} \mathbf{W}_{i,k}^* &= \mathbf{W}_{Ni}^*(\mathbf{z}_k) = \sum_m^N \hat{w}_{i,m}^*(\mathbf{z}_k) \Phi_m(\mathbf{z}_k), \\ f_{i,j,k}^* &= f_{Ni,j}^*(\mathbf{z}_k) = \sum_m^N \hat{f}_{i,j,m}^*(\mathbf{z}_k) \Phi_m(\mathbf{z}_k). \end{aligned} \quad (31)$$

Afterwards, the collision and forcing term are evaluated on collocation points via

$$(\mathbf{W}_\alpha)_{i,k}^{n+1} = (\mathbf{W}_\alpha)_{i,k}^* + \int_{t^n}^{t^{n+1}} (\mathbf{G}_\alpha)_{i,k}^W dt + \int_{t^n}^{t^{n+1}} (\mathbf{Q}_\alpha)_{i,k}^W dt, \quad (32)$$

and

$$(f_\alpha)_{i,j,k}^{n+1} = (f_\alpha)_{i,j,k}^* + \frac{1}{\Omega_j} \int_{t^n}^{t^{n+1}} \sum_{S_r \in \partial\Omega_j} S_r (F_\alpha)_{i,r,k}^f dt + \int_{t^n}^{t^{n+1}} (Q_\alpha)_{i,j,k}^f dt, \quad (33)$$

where $(F_\alpha)_r^f$ is the numerical flux at interface r in velocity space. In the solution algorithm loop, Eq. (32) can be solved first, and then the updated variables at t^{n+1} can be employed to evaluate the Maxwellian distribution in Eq. (33) implicitly. Similar treatment of hybrid Galerkin and collocation methods is also employed in [32].

For plasma transport, the evolution of electromagnetic field should be solved in a coupled way with flow field. The hybrid Galerkin-collocation method is employed as well, where the gPC coefficients are stepped to the intermediate state first,

$$\hat{\mathbf{M}}_i^* = \hat{\mathbf{M}}_i^n + \frac{1}{\Omega_i} \int_{t^n}^{t^{n+1}} \sum_r \Delta \mathbf{S}_r \cdot \hat{\mathbf{F}}_r^M dt, \quad (34)$$

where $\hat{\mathbf{F}}^M$ is the flux functions for the electromagnetic fields $(\hat{\mathbf{E}}, \hat{\mathbf{B}}, \hat{\phi}, \hat{\psi})$. Then the source terms are solved via,

$$\begin{aligned} \mathbf{E}_i^{n+1} &= \mathbf{E}_i^* - \frac{e}{\varepsilon_0} \int_{t^n}^{t^{n+1}} ((n\mathbf{U})_{ion} - (n\mathbf{U})_{ele}) dt, \\ \phi_i^{n+1} &= \phi_i^* + \frac{e}{\varepsilon_0} \int_{t^n}^{t^{n+1}} (n_{ion} - n_{ele}) dt. \end{aligned} \quad (35)$$

3.2. Fluxes computed using stochastic Galerkin

3.2.1. Plasma flux

Based on the finite volume framework, a scale-dependent interface flux function is needed in multi-scale modeling and simulation. Different from a purely upwind flux which loses efficiency in the collisional limit, we here develop a

kinetic central-upwind flux function based on an integral solution of the kinetic model equation. The integral solution originates from Kogan's monograph on rarefied gas dynamics [33] and has been employed by a series of gas-kinetic schemes [26,34–37]. Let us rewrite the stochastic BGK equation (16) for the gPC coefficients vector along the characteristics,

$$\frac{D\hat{\mathbf{f}}_\alpha}{Dt} + v_\alpha \hat{\mathbf{f}}_\alpha = v_\alpha \hat{\mathbf{m}}_\alpha. \quad (36)$$

We assume that the collision frequency v_α is kept fixed at the value that can be computed from the macroscopic variables at the previous timestep. Then the following integral solution holds along the characteristics,

$$\hat{\mathbf{f}}_\alpha(t, \mathbf{x}, \mathbf{u}) = v_\alpha \int_0^t \hat{\mathbf{m}}_\alpha(t', \mathbf{x}', \mathbf{u}') e^{-v_\alpha(t-t')} dt' + e^{-v_\alpha t} \hat{\mathbf{f}}_\alpha(0, \mathbf{x}^0, \mathbf{u}^0), \quad (37)$$

where $\mathbf{x}' = \mathbf{x} - \mathbf{u}'(t - t') - \frac{1}{2}\mathbf{a}(t - t')^2$ is the particle trajectory, and $\mathbf{x}^0 = \mathbf{x} - \mathbf{u}'t - \frac{1}{2}\mathbf{a}t^2$ is the location at initial time $t = 0$. The above solution indicates a self-conditioned mechanism for multi-scale gas dynamics. For example, when the evolving time t is much less than the mean collision time $\tau = 1/v_\alpha$, the latter term in Eq. (37) dominates and describes the free transport of particles. And if t is much larger than τ , the second term approaches to zero, and then the distribution function will be an accumulation of equilibrium state along the characteristic lines, which provides the underlying wave-propagation mechanism for hydrodynamic solutions. In the following, we present a detailed strategy for the construction of numerical fluxes. Since the electromagnetic force term \mathbf{a} is a stochastic variable, we do an operator splitting to evaluate fluxes in physical and velocity space.

With the simplified notations of physical cell interface $\mathbf{x}_{i+1/2} = 0$ and initial time $t^n = 0$, Eq. (37) along physical trajectories of particles can be rewritten into the following form,

$$\hat{\mathbf{f}}_\alpha(t, 0, \mathbf{u}_j) = v_\alpha \int_0^t \hat{\mathbf{m}}_\alpha(t', \mathbf{x}', \mathbf{u}_j) e^{-v_\alpha(t-t')} dt' + e^{-v_\alpha t} \hat{\mathbf{f}}_\alpha(0, -\mathbf{u}_j t, \mathbf{u}_j), \quad (38)$$

where $\hat{\mathbf{f}}_\alpha(0, -\mathbf{u}_j t, \mathbf{u}_j)$ is the initial distribution at each time step.

In the numerical scheme, the initial distribution function at cell interface can be obtained through reconstruction, i.e.,

$$(\hat{\mathbf{f}}_\alpha)(0, \pm 0, \mathbf{u}_j) = \begin{cases} (\hat{\mathbf{f}}_\alpha)_{i+1/2,j}^L, & x = 0^-, \\ (\hat{\mathbf{f}}_\alpha)_{i+1/2,j}^R, & x = 0^+. \end{cases} \quad (39)$$

The initial distributions $(\hat{\mathbf{f}}_\alpha)_{i+1/2,j}^{L,R}$ at the left and right hand sides of a cell interface are obtained through the van-Leer limiter.

The macroscopic conservative variables in the gPC expansions at the interface can be evaluated by taking moments over velocity space,

$$\hat{\mathbf{w}}_\alpha = \sum_{u_j > 0} (\hat{\mathbf{f}}_\alpha)_{i+1/2,j}^L \psi \Delta u_j + \sum_{u_j < 0} (\hat{\mathbf{f}}_\alpha)_{i+1/2,j}^R \psi \Delta u_j. \quad (40)$$

After that, we dive in the step 2 as illustrated in Sec. 2.3 and start evaluating the Maxwellian distribution function $\hat{\mathbf{m}}_\alpha$.

After all coefficients are obtained, the interface distribution function becomes

$$\hat{\mathbf{f}}_\alpha(t, 0, \mathbf{u}_j) = (1 - e^{-v_\alpha t}) (\hat{\mathbf{m}}_\alpha)_j + e^{-v_\alpha t} \left[(\hat{\mathbf{f}}_\alpha)_{i+1/2,j}^L H[\mathbf{u}_j] + (\hat{\mathbf{f}}_\alpha)_{i+1/2,j}^R (1 - H[\mathbf{u}_j]) \right], \quad (41)$$

where $H(\mathbf{u})$ is the Heaviside step function. Different from the two-side upwind flux evaluated from discontinuous $\hat{\mathbf{f}}_\alpha^L$ and $\hat{\mathbf{f}}_\alpha^R$, the Maxwellian distribution $\hat{\mathbf{m}}_\alpha$ takes the same value across the cell interface, evaluated from an average of left- and right-hand macroscopic variables. As analyzed in [38], the moments of it are equivalent as the results from central difference of macroscopic variables for well-resolved continuous flows. Therefore, the above interface distribution function can be regarded as a combination of central and upwind methods. With the variation of the ratio between evolving time t (i.e., the time step in the computation) and collision time $\tau_\alpha = 1/v_\alpha$, the factor $e^{-v_\alpha t}$ plays as a modulator and provides a self-adaptive solution between equilibrium and non-equilibrium physics.

After the coefficients of distribution function at all orders are determined, the corresponding gPC expansion can be expressed as,

$$f_{\alpha N}(t, 0, \mathbf{u}_j) = \sum_{m=0}^N \hat{f}_m(t, 0, \mathbf{u}_j) \Phi_m(\mathbf{z}), \quad (42)$$

and the corresponding fluxes of particle distribution function and conservative flow variables can be evaluated via

$$\begin{aligned} F_{\alpha N}^f(t, 0, \mathbf{u}_j, \mathbf{z}) &= \mathbf{u}_j f_{\alpha N}(t, 0, \mathbf{u}_j, \mathbf{z}), \\ \mathbf{F}_{\alpha N}^W(t, 0, \mathbf{z}) &= \int \mathbf{u} f_{\alpha N}(t, 0, \mathbf{u}, \mathbf{z}) \varpi d\mathbf{u} \simeq \sum_{j=0}^N w_j \mathbf{u}_j f_{\alpha N}(t, 0, \mathbf{u}_j, \mathbf{z}) \varpi_j, \end{aligned} \quad (43)$$

where \mathbf{u}_j denotes quadrature points in particle velocity space, and w_j is its integral weight in velocity space, and the time-integrated fluxes in Eq. (29) and (28) can be evaluated with respect to time in Eq. (41).

To validate the performance of the current central-upwind flux, we conduct a deterministic numerical experiment of shear layer [37] in the absence of electromagnetic evolution below. The initial condition of gas mixture is set as

$$(n, U, V, T) = \begin{cases} (1.33291 \times 10^{25}/m^3, 0, 408.05 \text{ m/s}, 400 \text{ K}), & x \leq 0 \\ (1.33291 \times 10^{25}/m^3, 0, -408.05 \text{ m/s}, 200 \text{ K}), & x > 0 \end{cases} \quad (44)$$

The reference Knudsen number of ion $\text{Kn}_i = \ell_0/L_0$ is 10^{-4} , with the ion mean free path being $\ell_0 = 10^{-7} \text{ m}$ and characteristic length $L_0 = 10^{-3} \text{ m}$. The reference temperature is $T_0 = 400 \text{ K}$, and the corresponding most probable speed is $C_0 = 2570.6 \text{ m/s}$. The mass ratio between ion and electron particles is set as $m_e/m_i = 0.05$ and collision time is $\tau_0 = 1.22 \times 10^{-11} \text{ s}$. The current central-upwind flux and pure upwind flux are compared in the numerical simulations with different physical cell numbers being used. The profiles of electron density, velocity and temperature at different time instants $t = \{t_c, 10t_c, 100t_c\}$, $t_c = \tau_0$ are presented in Fig. 2, while the references are the grid-converged solutions produced by the scheme [37]. As can be seen, compared with pure upwind flux, under different numerical resolutions, the current central-upwind flux invariably reduces the artificial dissipation effectively. It provides sharper flow structures on a relatively coarse mesh and ensures faster convergence of solutions.

3.2.2. Electromagnetic flux

Besides the flow variables, the numerical fluxes of electromagnetic fields in Eq. (27) are calculated by the wave-propagation method developed by Hakim et al. [39].

3.3. Fluxes and sources computed using stochastic collocation

Besides the construction of the interface flux, the source terms need to be evaluated inside each control volume within each time step. In this part, we show the detailed update algorithm for the collision and external force term with stochastic collocation method.

3.3.1. Macroscopic source terms

Given the intermediate macroscopic variables in the discrete cell $(\Omega_i, \Omega_j, \Omega_k)$, the macroscopic system writes as follows,

$$\begin{aligned} (\rho_\alpha \mathbf{U}_\alpha)_{i,k}^{n+1} &= (\rho_\alpha \mathbf{U}_\alpha)_{i,k}^* + \Delta t q_\alpha (n_\alpha (\mathbf{E} + \mathbf{U}_\alpha \times \mathbf{B}))_{i,k}^{n+1} + \int_{t^n}^{t^{n+1}} \left(v_\alpha \rho_\alpha (\bar{\mathbf{U}}_\alpha^* - \mathbf{U}_\alpha^*) \right)_{i,k} dt, \\ (\rho_\alpha \mathcal{E}_\alpha)_{i,k}^{n+1} &= (\rho_\alpha \mathcal{E}_\alpha)_{i,k}^* + \Delta t q_\alpha (n_\alpha \mathbf{E} \cdot \mathbf{U}_\alpha)_{i,k}^{n+1} + \int_{t^n}^{t^{n+1}} \left(v_\alpha (\rho_\alpha \bar{\mathcal{E}}_\alpha^* - \rho_\alpha \mathcal{E}_\alpha^*) \right)_{i,k} dt, \\ \mathbf{E}_{i,k}^{n+1} &= \mathbf{E}_{i,k}^* - \frac{e \Delta t}{\varepsilon_0} ((n \mathbf{U})_{ion} - (n \mathbf{U})_{ele})_{i,k}^{n+1}, \\ \phi_{i,k}^{n+1} &= \phi_{i,k}^* + \frac{e \Delta t}{\varepsilon_0} (n_{ion} - n_{ele})_{i,k}^{n+1}. \end{aligned} \quad (45)$$

We split the above system into two parts. First, the flow variables are evolved with respect to mixture source terms,

$$\begin{aligned} (\rho_\alpha \mathbf{U}_\alpha)_{i,k}^{**} &= (\rho_\alpha \mathbf{U}_\alpha)_{i,k}^* + \int_{t^n}^{t^{n+1}} \left(v_\alpha \rho_\alpha^{n+1} (\bar{\mathbf{U}}_\alpha^* - \mathbf{U}_\alpha^*) \right)_{i,k} dt, \\ (\rho_\alpha \mathcal{E}_\alpha)_{i,k}^{**} &= (\rho_\alpha \mathcal{E}_\alpha)_{i,k}^* + \int_{t^n}^{t^{n+1}} \left(v_\alpha \rho_\alpha^{n+1} (\bar{\mathcal{E}}_\alpha^* - \mathcal{E}_\alpha^*) \right)_{i,k} dt. \end{aligned} \quad (46)$$

The relaxation integrals are evaluated through the Rosenbrock method [40] to overcome possible stiffness.

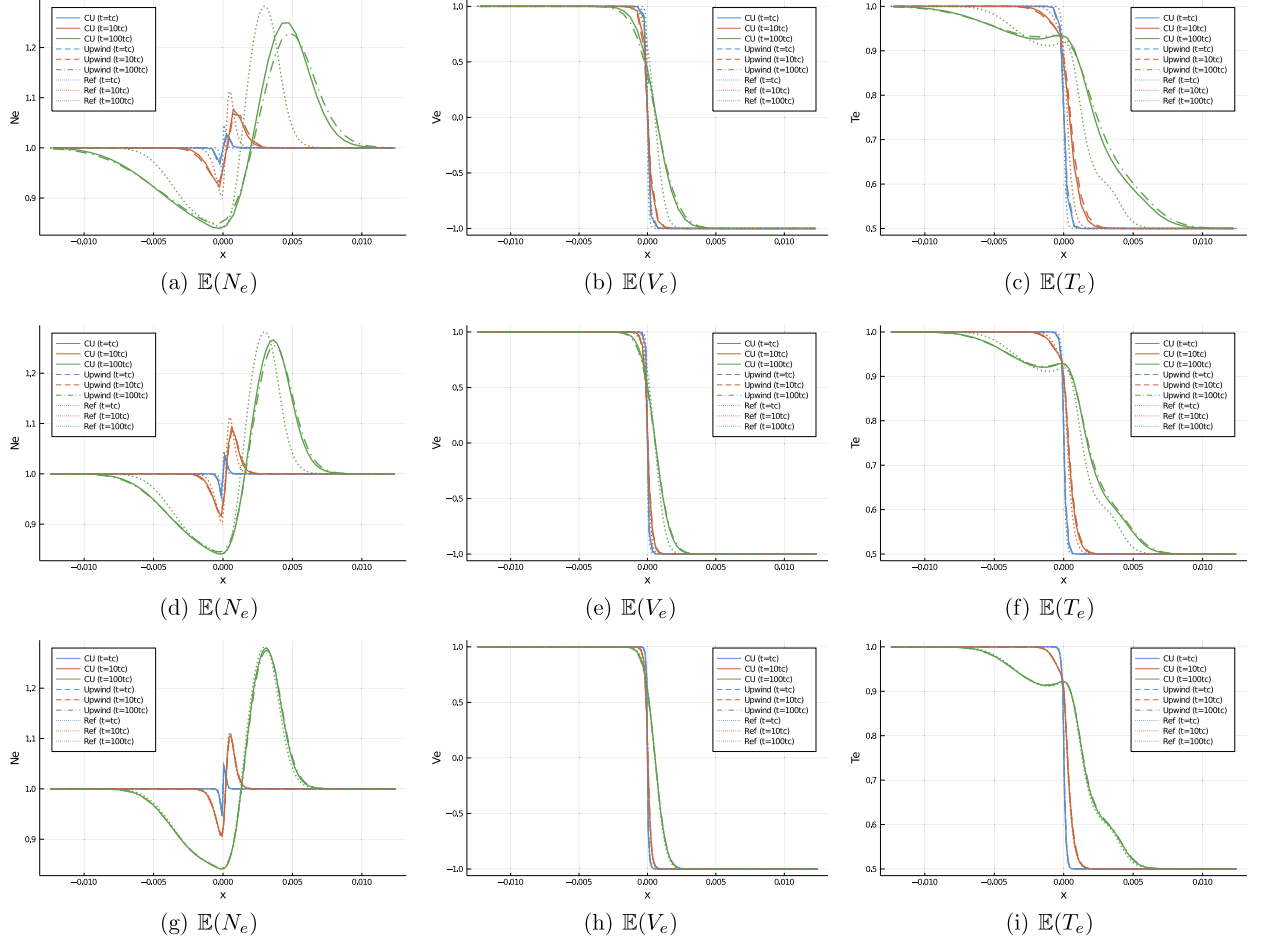


Fig. 2. Expectation values of N_e , V_e and T_e around the shear layer at different (row 1: $n_x = 200$, row 2: $n_x = 400$, row 3: $n_x = 800$). The profiles marked as "CU" are the current kinetic central-upwind solutions. (For interpretation of the colors in the figure(s), the reader is referred to the web version of this article.)

Then we solve the electromagnetic sources implicitly, in which a linear system can be solved, i.e.,

$$\begin{aligned} (\rho_\alpha \mathbf{U}_\alpha)_{i,k}^{n+1} &= (\rho_\alpha \mathbf{U}_\alpha)_{i,k}^{**} + \Delta t q_\alpha (n_\alpha (\mathbf{E} + \mathbf{U}_\alpha \times \mathbf{B}))_{i,k}^{n+1}, \\ (\rho_\alpha \mathcal{E}_\alpha)_{i,k}^{n+1} &= (\rho_\alpha \mathcal{E}_\alpha)_{i,k}^{**} + \Delta t q_\alpha (n_\alpha \mathbf{E} \cdot \mathbf{U}_\alpha)_{i,k}^{n+1}, \\ \mathbf{E}_{i,k}^{n+1} &= \mathbf{E}_{i,k}^* - \frac{e \Delta t}{\varepsilon_0} ((n \mathbf{U})_{ion} - (n \mathbf{U})_{ele})_{i,k}^{n+1}, \\ \phi_{i,k}^{n+1} &= \phi_{i,k}^* + \frac{e \Delta t}{\varepsilon_0} (n_{ion} - n_{ele})_{i,k}^{n+1}. \end{aligned} \quad (47)$$

3.3.2. Particle distribution function

The updated macroscopic variables can be used to step the particle distribution functions of ion and electron implicitly. Let us consider the kinetic equation,

$$\frac{\partial f_\alpha}{\partial t} + \mathbf{a}_\alpha \cdot \nabla_{\mathbf{u}} f_\alpha = v_\alpha (\mathcal{M}_\alpha - f_\alpha), \quad (48)$$

where the electromagnetic force is

$$\mathbf{a}_\alpha = \frac{q_\alpha}{m_\alpha} (\mathbf{E}^{n+1} + \mathbf{u}_\alpha \times \mathbf{B}^{n+1}).$$

Making the simplified notations of velocity cell interface $\mathbf{u}_{j+1/2} = 0$ and initial time $t^n = 0$ again, we write the integral solution of Eq. (48) as,

$$\begin{aligned} f_\alpha(t, \mathbf{x}_i, 0, \mathbf{z}_k) &= v_\alpha \int_0^t \mathcal{M}_\alpha^*(t', \mathbf{x}_i, \mathbf{u}', \mathbf{z}_k) e^{-v_\alpha(t-t')} dt' + e^{-v_\alpha t} f_\alpha^*(0, \mathbf{x}_i, -\mathbf{a}_\alpha t, \mathbf{z}_k) \\ &= \mathcal{M}_\alpha^*(0, \mathbf{x}, \mathbf{u} - \mathbf{a}_\alpha t, \mathbf{z}_k) (1 - e^{-v_\alpha t}) + f_\alpha^*(0, \mathbf{x}_i, \mathbf{u} - \mathbf{a}_\alpha t, \mathbf{z}_k) e^{-v_\alpha t}. \end{aligned} \quad (49)$$

Similar to physical space, the above interface distribution function can also be regarded as a combination of central difference and upwind methods in particle velocity space. With the variation of the ratio between evolving time t (i.e., the time step in the computation) and collision time $\tau_\alpha = 1/v_\alpha$, it provides a self-adaptive solution from equilibrium to non-equilibrium. Based the above solution, the interface flux in particle velocity space can be constructed as

$$F_\alpha^f(t, \mathbf{x}_i, 0, \mathbf{z}_k) = \mathbf{a}_\alpha f_\alpha(t, \mathbf{x}_i, 0, \mathbf{z}_k), \quad (50)$$

and the time-integrated flux can be evaluated directly with respect to t .

For the collision term, with the updated flow variables at t^{n+1} , an implicit update can be arranged. Therefore, the update algorithm of particle distribution function can be written as,

$$(f_\alpha)_{i,j,k}^{n+1} = (f_\alpha)_{i,j,k}^* + \frac{1}{\Omega_j} \int_{t^n}^{t^{n+1}} \sum_{S_r \in \partial \Omega_j} S_r (F_\alpha)_{i,r,k}^f dt + \Delta t v_\alpha^{n+1} \left((\mathcal{M}_\alpha)_{i,j,k}^{n+1} - (f_\alpha)_{i,j,k}^{n+1} \right). \quad (51)$$

3.4. Time step

In the current scheme, the time step is determined by the Courant-Friedrichs-Lowy condition in phase space,

$$\Delta t = C \min \left(\frac{\min(|\Delta \mathbf{x}|)}{\max(|\mathbf{u}|) + \max(|\mathbf{U}|)}, \frac{\min(|\Delta \mathbf{x}|)}{c}, \frac{\min(|\Delta \mathbf{u}|)}{\max(|\mathbf{a}|)} \right), \quad (52)$$

where C is the CFL number, $\mathbf{u} = (\mathbf{u}_{ion}, \mathbf{u}_{ele})$ is particle velocity, $\mathbf{U} = (\mathbf{U}_{ion}, \mathbf{U}_{ele})$ is fluid velocity, and c is speed of light. In the computation, c usually takes a pseudo value which is less than 3.0×10^8 m/s but a few orders larger than particle velocity.

3.5. Asymptotic analysis

In this part we will present theoretical analysis on the current model and numerical algorithm, with special focus on their asymptotic limits.

3.5.1. Asymptotic limits of the BGK-Maxwell system

Let us first consider the BGK equation under electromagnetic force fields. From Eq. (6), we see that the collision frequency is positively correlated with plasma density and temperature. If the plasma gets more rarefied and cooler, the intensity of collision term decreases correspondingly. As the collision frequency v_α approaches zero, the BGK equation automatically reduces to the Vlasov equation, i.e.,

$$\frac{\partial f_\alpha}{\partial t} + \mathbf{u} \cdot \nabla_{\mathbf{x}} f_\alpha + \frac{q_\alpha}{m_\alpha} (\mathbf{E} + \mathbf{u} \times \mathbf{B}) \cdot \nabla_{\mathbf{u}} f_\alpha = 0. \quad (53)$$

On the other hand, as the collision frequency increases, the two-fluid system (8) can be obtained from the BGK equation and describes the motions of plasma as fluid. With the quasineutral assumption $n_i \simeq n_e$, we can get the generalized Ohm's law from the momentum transport equation,

$$\begin{aligned} \mathbf{E} + \mathbf{U} \times \mathbf{B} &= \eta \mathbf{J} + \frac{1}{e\rho} \left[\frac{m_{ion} m_{ele} n}{e} \frac{\partial}{\partial t} \left(\frac{\mathbf{J}}{n} \right) \right. \\ &\quad \left. + (m_{ion} - m_{ele}) \mathbf{J} \times \mathbf{B} + m_{ele} \nabla_{\mathbf{x}} p_{ion} - m_{ion} \nabla_{\mathbf{x}} p_{ele} \right] \end{aligned} \quad (54)$$

where $\mathbf{J} = -ne(\mathbf{U}_{ele} - \mathbf{U}_{ion})$ is the current and $\eta = m_{ele} v_{ie}/ne^2$ is the resistivity. The relative materiality of the terms in the above equation can be evaluated through dimension analysis. Let us introduce the following dimensionless variables,

$$\begin{aligned} \tilde{\mathbf{x}} &= \frac{\mathbf{x}}{L_0}, \tilde{t} = \frac{t}{L_0/U_0}, \tilde{m} = \frac{m}{m_{ion}}, \tilde{n} = \frac{n}{n_0}, \tilde{\mathbf{U}} = \frac{\mathbf{U}}{U_0}, \\ \tilde{\mathbf{B}} &= \frac{\mathbf{B}}{B_0}, \tilde{\mathbf{E}} = \frac{\mathbf{E}}{B_0 U_0}, \tilde{\mathbf{J}} = \frac{\mathbf{J}}{en_0 U_0}, \tilde{r}_g = \frac{r_g}{L_0}, \end{aligned}$$

and the Ohm's law becomes

$$\tilde{\mathbf{E}} + \tilde{\mathbf{U}} \times \tilde{\mathbf{B}} = \tilde{r}_g \tilde{\eta} \tilde{\mathbf{J}} + \frac{\tilde{m}_{ele} \tilde{r}_g}{1 + \tilde{m}_{ele}} \frac{\partial}{\partial \tilde{t}} \left(\frac{\tilde{\mathbf{J}}}{\tilde{n}} \right) + \frac{1 - \tilde{m}_{ele}}{\tilde{n}_e} \tilde{\mathbf{J}} \times \tilde{\mathbf{B}} - \frac{\tilde{r}_g}{\tilde{n}_e} (\nabla_{\tilde{\mathbf{x}}} \tilde{p}_{ele} - \tilde{m}_{ele} \nabla_{\tilde{\mathbf{x}}} \tilde{p}_{ion}). \quad (55)$$

As is shown, except for the Hall current, the rest three terms are proportional to the gyroradius. Simplifications could be made based on the Ohm's law. For example, in slow motions where inertial (i.e., cyclotron frequency) effects are unimportant, the term of time derivative can be neglected. In the limit $m_{ele}/m_{ion} \rightarrow 0$ and $\nu_i, \nu_e \gg 0$, the two-fluid system can be degenerated to single-fluid Hall-MHD equations,

$$\begin{aligned} \frac{\partial \rho}{\partial t} + \nabla_{\mathbf{x}} \cdot (\rho \mathbf{U}) &= 0, \\ \frac{\partial(\rho \mathbf{U})}{\partial t} + \nabla_{\mathbf{x}} \cdot (\rho \mathbf{U} \mathbf{U}) &= -\nabla_{\mathbf{x}} p + \mathbf{J} \times \mathbf{B}, \\ \frac{\partial(\rho \mathcal{E})}{\partial t} + \nabla_{\mathbf{x}} \cdot (\rho \mathcal{E} \mathbf{U}) &= \nabla_{\mathbf{x}} \cdot (p \mathbf{U}) + \mathbf{J} \cdot \mathbf{E}, \\ \mathbf{E} + \mathbf{U} \times \mathbf{B} &= \eta \mathbf{J} + \frac{1}{en} (\mathbf{J} \times \mathbf{B} - \nabla_{\mathbf{x}} p_{ele}), \\ \frac{\partial \sigma}{\partial t} + \nabla_{\mathbf{x}} \cdot \mathbf{J} &= 0, \end{aligned} \quad (56)$$

where σ is electric charge density. Together with Maxwell's equations, this set is able to describe the equilibrium state of the plasma.

The Hall-MHD equations can be further simplified. Since the resistivity coefficient η is proportional to the collision frequency between ions and electrons, as $\nu_{ie} \rightarrow 0$, the plasma will become fully conductive. If the gyroradius approaches zero, and the contributions from Hall effects are minor to be neglected, then in this regime the Ohm's law is simply as

$$\mathbf{E} + \mathbf{U} \times \mathbf{B} = 0. \quad (57)$$

Common MHD applications are concerned about the situation where the fluid velocity is much smaller than the speed of light. Neglecting the displacement current in the Ampere's law of the Maxwell's equations, the current can be expressed in terms of magnetic intensity,

$$\mathbf{J} = \frac{1}{\nu_0} \nabla_{\mathbf{x}} \times \mathbf{B}, \quad (58)$$

and we get the ideal MHD equations,

$$\begin{aligned} \frac{\partial \rho}{\partial t} + \nabla_{\mathbf{x}} \cdot (\rho \mathbf{U}) &= 0, \\ \frac{\partial(\rho \mathbf{U})}{\partial t} + \nabla_{\mathbf{x}} \cdot (\rho \mathbf{U} \mathbf{U}) &= -\nabla_{\mathbf{x}} p + \frac{(\mathbf{B} \cdot \nabla_{\mathbf{x}}) \mathbf{B}}{\mu_0} - \nabla_{\mathbf{x}} \left(\frac{\mathbf{B}^2}{2\mu_0} \right), \\ \frac{\partial(\rho \mathcal{E})}{\partial t} + \nabla_{\mathbf{x}} \cdot (\rho \mathcal{E} \mathbf{U}) &= \nabla_{\mathbf{x}} \cdot (p \mathbf{U}) + \frac{1}{\mu_0} \rho \mathbf{U} \cdot (\nabla_{\mathbf{x}} \times \mathbf{B} \times \mathbf{B}), \\ \frac{\partial \mathbf{B}}{\partial t} + \nabla_{\mathbf{x}} \times (\mathbf{U} \times \mathbf{B}) &= 0. \end{aligned} \quad (59)$$

In contrast to the ideal MHD regime, we can also consider the non-conductive limit where the interspecies molecular interaction is intensive with $\nu_{ie} \rightarrow \infty$. As the resistivity approaches infinity, all the current-related terms vanish, and the plasma now behaves like dielectric material,

$$\frac{\partial f_\alpha}{\partial t} + \mathbf{u} \cdot \nabla_{\mathbf{x}} f_\alpha = \nu_\alpha (\mathcal{M}_\alpha - f_\alpha), \quad f_\alpha \equiv \mathcal{M}_\alpha, \quad (60)$$

and the upscaling two-fluid system deduces to the Euler equations,

$$\begin{aligned} \frac{\partial \rho}{\partial t} + \nabla_{\mathbf{x}} \cdot (\rho \mathbf{U}) &= 0, \\ \frac{\partial(\rho \mathbf{U})}{\partial t} + \nabla_{\mathbf{x}} \cdot (\rho \mathbf{U} \mathbf{U}) &= -\nabla_{\mathbf{x}} p, \\ \frac{\partial(\rho \mathcal{E})}{\partial t} + \nabla_{\mathbf{x}} \cdot (\rho \mathcal{E} \mathbf{U}) &= \nabla_{\mathbf{x}} \cdot (p \mathbf{U}). \end{aligned} \quad (61)$$

3.5.2. Interface fluxes

Besides the theoretical modeling, the asymptotic preserving property for the limiting solutions is also a preferred nature for the kinetic scheme. Let us consider the interface fluxes constructed in Sec. 3.2 and 3.3 first. In the collisionless limit where v_α approaches zero, the relation $v_\alpha \Delta t \ll 1$ holds naturally, and the collision term in Eq. (1) disappears. In this case, the interface distribution function in both Eq. (41) and (49) go to the non-equilibrium distribution parts. For brevity, we write them down into collocation form, i.e.,

$$\begin{aligned} (f_\alpha)_{i+1/2,j,k} &= (f_\alpha)_{i+1/2,j,k}^L H(\mathbf{u}_j) + (f_\alpha)_{i+1/2,j,k}^R (1 - H(\mathbf{u}_j)), \\ (f_\alpha)_{i,j+1/2,k} &= f_\alpha^*(\mathbf{x}_i, \mathbf{u}_j - \mathbf{a}_\alpha t, \mathbf{z}_k), \end{aligned} \quad (62)$$

and the update algorithm reduces to

$$\begin{aligned} (f_\alpha)_{i,j,k}^{n+1} &= (f_\alpha)_{i,j,k}^n + \frac{\Delta t}{\Omega_i} \mathbf{u}_j \left((f_\alpha)_{i-1/2,j,k}^L H[\mathbf{u}_j] + (f_\alpha)_{i-1/2,j,k}^R (1 - H[\mathbf{u}_j]) \right) \\ &\quad - \frac{\Delta t}{\Omega_i} \mathbf{u}_j \left((f_\alpha)_{i+1/2,j,k}^L H[\mathbf{u}_j] + (f_\alpha)_{i+1/2,j,k}^R (1 - H[\mathbf{u}_j]) \right) \\ &\quad + \frac{\Delta t}{\Omega_i} \mathbf{a}_j \left((f_\alpha)_{i,j-1/2,k}^* - (f_\alpha)_{i,j+1/2,k}^* \right), \end{aligned} \quad (63)$$

which constitutes a fully upwind scheme for the Vlasov equation.

On the other hand, in the hydrodynamic regime with intensive collisions, the interface distribution becomes,

$$\begin{aligned} (f_\alpha)_{i+1/2,j,k} &= (\mathcal{M}_\alpha)_{i+1/2,j}, \\ (f_\alpha)_{i,j+1/2,k} &= \mathcal{M}_\alpha^*(\mathbf{x}_i, \mathbf{u} - \mathbf{a}_\alpha t, \mathbf{z}_k), \end{aligned} \quad (64)$$

leading to near-equilibrium MHD or Euler solutions.

3.5.3. Source terms

Besides the flux functions, the treatment of source terms plays an important role for the asymptotic property of scheme. Let us rewrite the electromagnetic sources in Eq. (47) as follows,

$$\begin{aligned} (\rho_{ion} \mathbf{U}_{ion})_{i,k}^{n+1} &= (\rho_{ion} \mathbf{U}_{ion})_{i,k}^{**} + \Delta t e (n_{ion} (\mathbf{E} + \mathbf{U}_{ion} \times \mathbf{B}))_{i,k}^{n+1}, \\ (\rho_{ele} \mathbf{U}_{ele})_{i,k}^{n+1} &= (\rho_{ele} \mathbf{U}_{ele})_{i,k}^{**} - \Delta t e (n_{ele} (\mathbf{E} + \mathbf{U}_{ele} \times \mathbf{B}))_{i,k}^{n+1}, \\ (\rho_{ion} \mathcal{E}_{ion})_{i,k}^{n+1} &= (\rho_{ion} \mathcal{E}_{ion})_{i,k}^{**} + \Delta t e (n_{ion} \mathbf{E} \cdot \mathbf{U}_{ion})_{i,k}^{n+1}, \\ (\rho_{ele} \mathcal{E}_{ele})_{i,k}^{n+1} &= (\rho_{ele} \mathcal{E}_{ele})_{i,k}^{**} - \Delta t e (n_{ele} \mathbf{E} \cdot \mathbf{U}_{ele})_{i,k}^{n+1}, \\ \mathbf{E}_{i,k}^{n+1} &= \mathbf{E}_{i,k}^* - \frac{e \Delta t}{\epsilon_0} (n_{ion} \mathbf{U}_{ion} - n_{ele} \mathbf{U}_{ele})_{i,k}^{n+1}, \\ \phi_{i,k}^{n+1} &= \phi_{i,k}^* + \frac{e \Delta t}{\epsilon_0} (n_{ion} - n_{ele})_{i,k}^{n+1}, \end{aligned} \quad (65)$$

where the asterisk * and ** denote intermediate variables updated from interface fluxes and mechanical collision terms.

Adding the momentum and energy equations of ion and electron, we get

$$\begin{aligned} (\rho \mathbf{U})_{i,k}^{n+1} - (\rho \mathbf{U})_{i,k}^{**} &= \Delta t e ((n_{ion} - n_{ele}) \mathbf{E})_{i,k}^{n+1} + \Delta t (\mathbf{J}_{ion} + \mathbf{J}_{ele}) \times \mathbf{B}_{i,k}^{n+1}, \\ &= \Delta t (\sigma \mathbf{E})_{i,k}^{n+1} + \Delta t (\mathbf{J} \times \mathbf{B})_{i,k}^{n+1}, \\ (\rho \mathcal{E})_{i,k}^{n+1} - (\rho \mathcal{E})_{i,k}^{**} &= \Delta t ((\mathbf{J}_{ion} + \mathbf{J}_{ele}) \cdot \mathbf{E})_{i,k}^{n+1} = \Delta t (\mathbf{J} \cdot \mathbf{E})_{i,k}^{n+1}. \end{aligned} \quad (66)$$

So far no any assumptions are introduced, and let us multiply the first equation in Eq. (65) by m_{ele} and second by m_{ion} , subtract the latter from the former and consider the quasineutral ansatz, we come to

$$\begin{aligned} m_{ion} m_{ele} (n (\mathbf{U}_{ion} - \mathbf{U}_{ele}))_{i,k}^{n+1} - m_{ion} m_{ele} (n (\mathbf{U}_{ion} - \mathbf{U}_{ele}))_{i,k}^{**} \\ = \Delta t e (m_{ion} + m_{ele}) (n \mathbf{E})_{i,k}^{n+1} + \Delta t e (n (m_{ele} \mathbf{U}_{ion} + m_{ion} \mathbf{U}_{ele}) \times \mathbf{B})_{i,k}^{n+1}. \end{aligned} \quad (67)$$

The results above can be simplified under specific conditions. Now let us suppose $m_{ion} \gg m_{ele}$ and recover \mathbf{J}^* from \mathbf{J}^{**} as described in Eq. (45), the transport equations of plasma mixture in the collocation form can be written as

$$\begin{aligned}
\rho_{i,k}^{n+1} &= \rho_{i,k}^n + \frac{1}{\Omega_i} \int_{t^n}^{t^{n+1}} m_{ion} \mathbf{u} ((f_{ion})_{i-1/2,k} - (f_{ion})_{i+1/2,k}) d\mathbf{u}, \\
(\rho \mathbf{U})_{i,k}^{n+1} &= (\rho \mathbf{U})_{i,k}^n + \frac{1}{\Omega_i} \int_{t^n}^{t^{n+1}} m_{ion} \mathbf{u}^2 ((f_{ion})_{i-1/2,k} - (f_{ion})_{i+1/2,k}) d\mathbf{u} + \Delta t (\mathbf{J} \times \mathbf{B})_{i,k}^{n+1}, \\
(\rho \mathcal{E})_{i,k}^{n+1} &= (\rho \mathcal{E})_{i,k}^n + \frac{1}{\Omega_i} \int_{t^n}^{t^{n+1}} m_{ion} \frac{1}{2} \mathbf{u}^3 ((f_{ion})_{i-1/2,k} - (f_{ion})_{i+1/2,k}) d\mathbf{u} + \Delta t (\mathbf{J} \cdot \mathbf{E})_{i,k}^{n+1}, \\
\mathbf{E}_{i,k}^{n+1} + \mathbf{U}_{i,k}^{n+1} \times \mathbf{B}_{i,k}^{n+1} &= \eta_{i,k}^{n+1} \mathbf{J}_{i,k}^{n+1} + \frac{1}{e \rho_{i,k}^{n+1}} \left(\frac{m_{ion} m_{ele}}{e} \frac{\mathbf{J}_{i,k}^{n+1} - \mathbf{J}_{i,k}^*}{\Delta t} + m_{ion} \mathbf{J}_{i,k}^{n+1} \times \mathbf{B}_{i,k}^{n+1} \right),
\end{aligned} \tag{68}$$

where the last equation is the generalized Ohm's law. As analyzed in Sec. 3.5.1, the first term is related to the first-order effect of gyroradius. In slow motions where the cyclotron frequency is much larger than the characteristic frequency of the system, the gyroradius approaches zero, and the contribution from current derivative becomes ignorable. Let $\nu_{ie} \rightarrow 0$ with fully conductive assumption, and consider the ideal MHD limit where the Hall current term is minor, we then get the ideal Ohm's law,

$$\mathbf{E}_{i,k}^{n+1} + \mathbf{U}_{i,k}^{n+1} \times \mathbf{B}_{i,k}^{n+1} = 0, \tag{69}$$

and Eq. (68) deduces to the ideal MHD equations.

3.6. Summary

The flowchart of the current solution algorithm is summarized in Fig. 3.

4. Numerical experiments

In this section, we will present some numerical results. The goal of numerical experiments is not simply to validate the performance of the current scheme, but also to present and analyze new physical observations. In order to demonstrate the multi-scale nature of the algorithm, simulations from Vlasov to magnetohydrodynamics (MHD) regimes are presented. The following dimensionless flow variables are introduced in the simulations,

$$\begin{aligned}
\tilde{\mathbf{x}} &= \frac{\mathbf{x}}{L_0}, \tilde{t} = \frac{t}{L_0/U_0}, \tilde{m} = \frac{m}{m_{ion}}, \tilde{n} = \frac{n}{n_0}, \tilde{\mathbf{U}} = \frac{\mathbf{U}}{U_0}, \tilde{T} = \frac{T}{T_0}, \\
\tilde{\mathbf{P}} &= \frac{\mathbf{P}}{m_{ion} n_0 U_0^2}, \tilde{\mathbf{q}} = \frac{\mathbf{q}}{m_{ion} n_0 U_0^3}, \tilde{f} = \frac{f}{n_0 U_0^3}, \tilde{\mathbf{u}} = \frac{\mathbf{u}}{U_0}, \tilde{q}_\alpha = \frac{q_\alpha}{e}, \\
\tilde{\mathbf{B}} &= \frac{\mathbf{B}}{B_0}, \tilde{\mathbf{E}} = \frac{\mathbf{E}}{B_0 U_0}, \tilde{\sigma} = \frac{\sigma}{en_0}, \tilde{\mathbf{J}} = \frac{\mathbf{J}}{en_0 U_0}, \tilde{r_g} = \frac{r_g}{L_0}, \tilde{\lambda_D} = \frac{\lambda_D}{r_g},
\end{aligned}$$

where $U_0 = \sqrt{k_B T_0 / m_{ion}}$ is the thermal velocity of ions, $\lambda_D = \sqrt{\varepsilon_0 k_B T_0 / n_0 e^2}$ is the Debye length, and $r_g = m_{ion} U_0 / e B_0$ is the gyroradius of ion in the reference state. For brevity, the tilde notation for dimensionless variables will be removed henceforth. Therefore, the dimensionless BGK-Maxwell system becomes,

$$\begin{aligned}
\frac{\partial f_\alpha}{\partial t} + \mathbf{u} \cdot \nabla_{\mathbf{x}} f_\alpha + \frac{1}{r_g m_\alpha} (\mathbf{E} + \mathbf{u} \times \mathbf{B}) \cdot \nabla_{\mathbf{u}} f_\alpha &= v_\alpha (\mathcal{M}_\alpha - f_\alpha), \\
\frac{\partial \mathbf{E}}{\partial t} - c^2 \nabla_{\mathbf{x}} \times \mathbf{B} &= -\frac{1}{\lambda_D^2 r_g} \mathbf{J}, \\
\frac{\partial \mathbf{B}}{\partial t} + \nabla_{\mathbf{x}} \times \mathbf{E} &= 0, \\
\frac{1}{\chi} \frac{\partial \phi}{\partial t} + \nabla_{\mathbf{x}} \cdot \mathbf{E} &= \frac{\sigma}{\lambda_D^2 r_g}, \\
\frac{1}{c^2 \gamma} \frac{\partial \psi}{\partial t} + \nabla_{\mathbf{x}} \cdot \mathbf{B} &= 0.
\end{aligned} \tag{70}$$

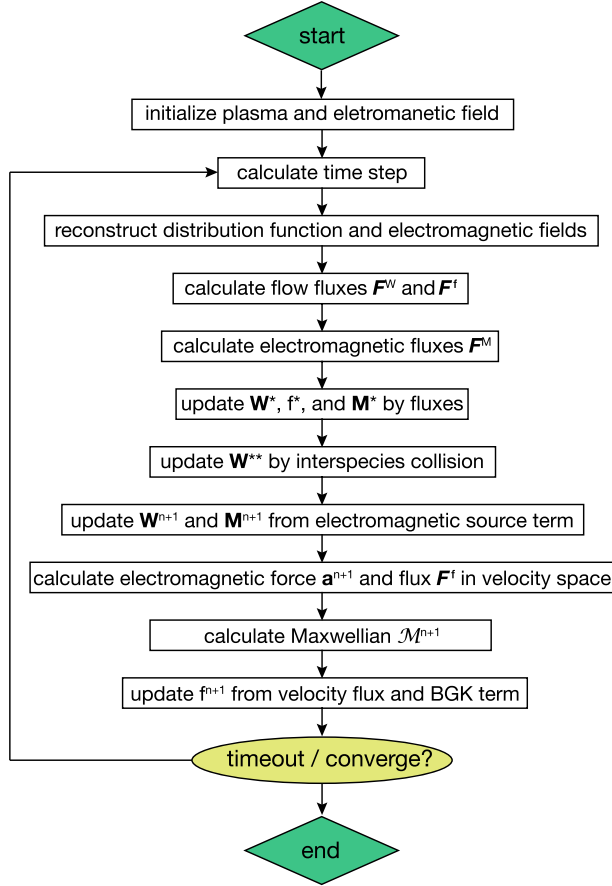


Fig. 3. Flowchart of solution algorithm.

4.1. Landau damping

The Landau damping is a physical phenomenon first predicted by Landau [41] based on theoretical derivation, namely the exponential decay effect of electromagnetic waves in collisionless plasmas. Here, we use the example of Landau damping to verify the performance of the current stochastic scheme in the Vlasov limit. For brevity, we consider the one-dimensional case first, and thus the Maxwell's equations for the electrostatic field degenerates into the Poisson equation for the electric potential.

4.1.1. Linear case

Consider the following macroscopic system

$$\begin{bmatrix} n_{ion} \\ n_{ele} \\ U \\ T \end{bmatrix}_{t=0} = \begin{bmatrix} 1 \\ 1 + \alpha\xi \cos(kx) \\ 0 \\ 1 \end{bmatrix},$$

where α is the amplitude of electromagnetic wave, k is the wave number, and ξ is a random parameter. The corresponding particle distribution functions at $t = 0$ are the Maxwellian,

$$f_\alpha = n_\alpha \left(\frac{m_\alpha}{2\pi T} \right)^{1/2} \exp \left(-\frac{m_\alpha}{2T} (u - U)^2 \right).$$

The computational setup is listed in Table 1. Given the minor amplitude α , the Vlasov-Poisson system can be regarded as the Maxwellian plus linearized perturbation near equilibrium. With the large mass ratio, we fix the slow motions of ions as background, and solve the evolution of electrons. The standard non-intrusive stochastic collocation method is also employed to provide reference solution. Besides, the damping rate of electric field energy can be derived by linear theory [5]. We hereby combine α and ξ into a new perturbation amplitude β , and derive the following relation as benchmark,

Table 1
Computational setup of linear Landau damping.

t	x	N_x	m_{ion}/m_{ele}	u_{ele}	N_u	α
(0, 40]	$[-\pi/k, \pi/k]$	128	1836	$[-5, 5]$	128	0.01
k	ξ	Polynomial	$N_z(gPC)$	$N_z(\text{quad})$	Kn	cfl
0.5	$\mathcal{U}(0, 1)$	Legendre	5	9	100	0.2

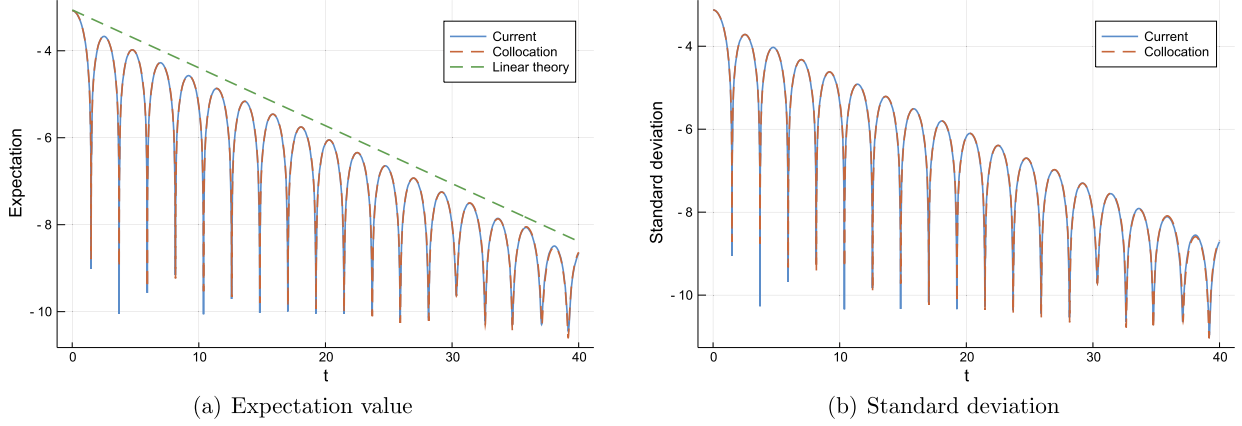


Fig. 4. Expectation value and standard deviation of electric field energy (logarithmic) in linear Landau damping.

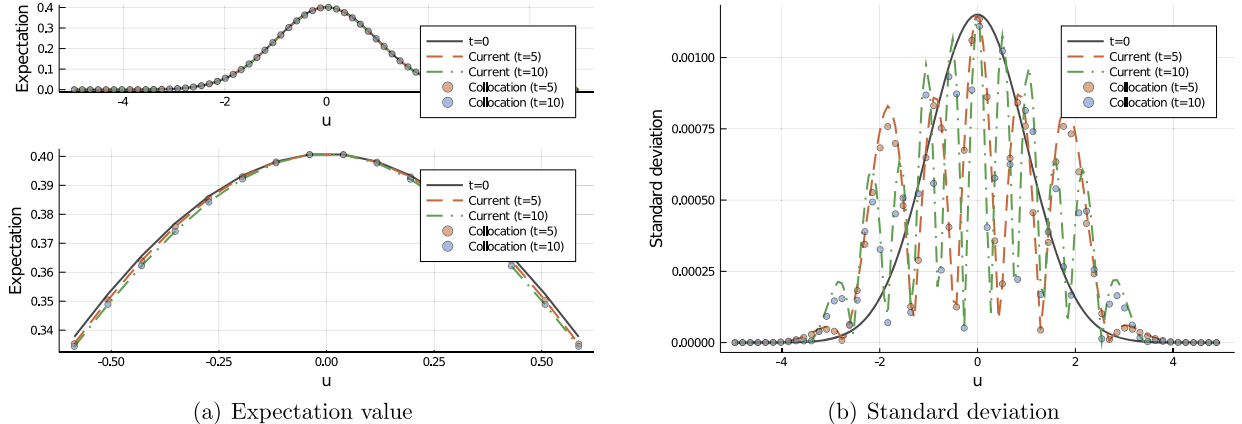


Fig. 5. Time evolved expectation value and standard deviation of particle distribution function at $x = 0$ in linear Landau damping.

$$\mathcal{E}(x, t) \simeq 4\beta \times 0.3677e^{-0.1533t} \sin(kx) \cos(1.4156t - 0.536245). \quad (71)$$

Fig. 4 presents the time evolution of electric energy. As is shown, the current stochastic kinetic scheme provides equivalent numerical solution as the standard collocation method. The expected energy damping rate is consistent with the theoretical damping rate -0.1533 , and the oscillation frequency of the electromagnetic wave corresponds well to the theoretical value $\omega = 1.4156$.

Besides the evolution of expectation value, the stochastic scheme provides the opportunity to study the uncertainty propagation modes simultaneously. As shown in Fig. 4(b), the uncertainties travel along with the structure of electromagnetic wave and present similar evolution patterns with mean field. The magnitudes of expectation and variance are on the same order due to the small perturbation strength.

Fig. 5 presents the time evolution of particle distribution function at the domain center $x = 0$. From the zoom-in expected distribution function around $u = 0$, we see that the low-speed particles resonate with the electromagnetic wave and gradually absorb energy, resulting in decreased value of particle distribution. In spite of the minor variation of expected value around the Maxwellian for the linear damping case, the standard deviation of solutions shows an increasingly symmetric oscillation in the velocity space during the resonance process. It indicates a more significant sensitivity compared to the mean field, and provides a quantitative description of the non-equilibrium effects triggered by the particle-wave resonance.

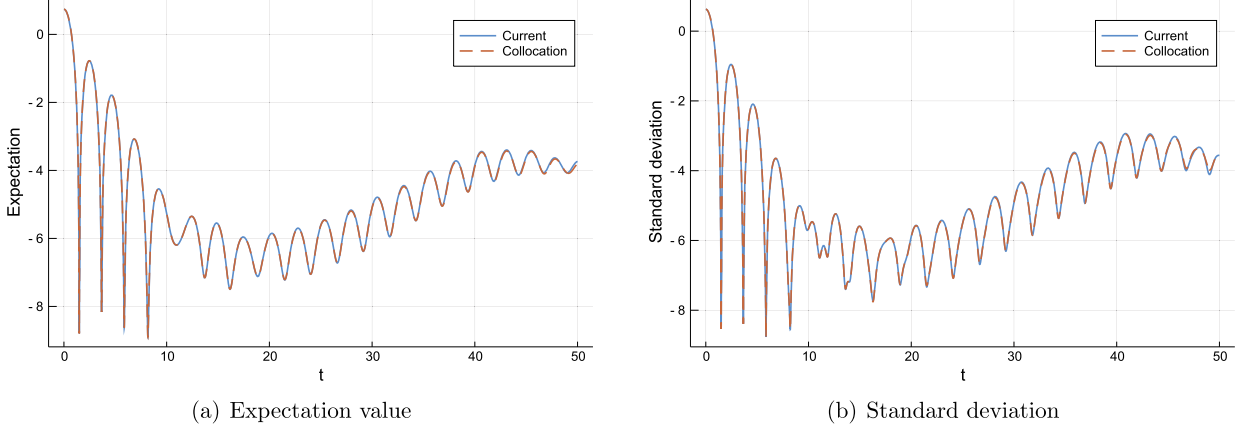


Fig. 6. Expectation value and standard deviation of electric field energy (logarithmic) in nonlinear Landau damping.

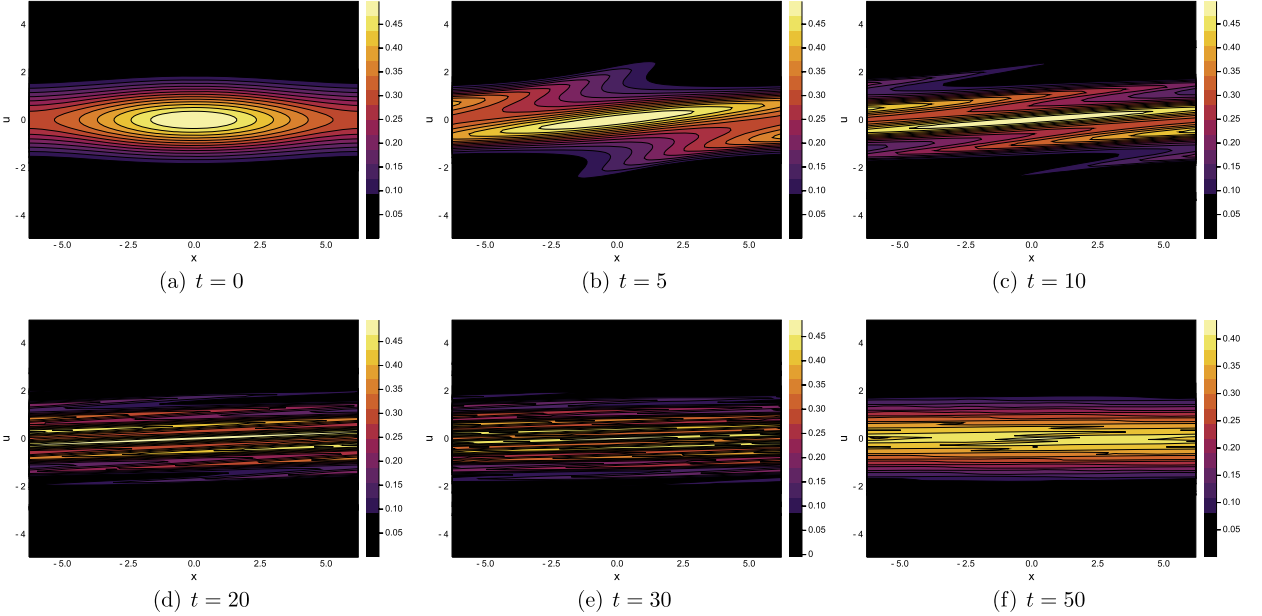


Fig. 7. Time evolved expectation value of particle distribution function over phase space (x, u) in nonlinear Landau damping.

4.1.2. Nonlinear case

The same initial conditions and computational setups as linear case are followed, except for the enhanced amplitude $\alpha = 0.5$. The evolution of electric energy is presented in Fig. 6. As the amplitude of the electromagnetic wave increases, nonlinear effects would emerge correspondingly, resulting in a rise in energy after the initial damping.

Fig. 7 shows the time evolution of expected particle distribution over the phase space (x, u), and Fig. 8 picks out the expectation and variance of particle distribution at physical domain center $x = 0$. Given the increasing intensity of radio field, here the particle distribution function is deformed in phase space. Consistent with the linear case, the change of variance here is more significant than expectation value, indicating a stronger sensibility.

4.2. Two-stream instability

The two-stream instability is another typical phenomenon in collisionless plasmas. To a certain extent, it can also be regarded as an inverse phenomenon of Landau damping.

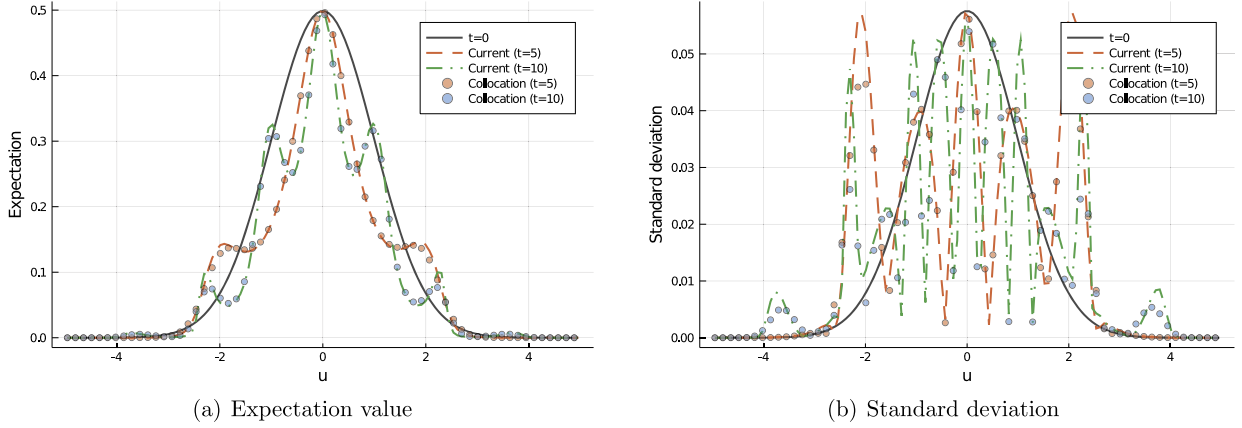


Fig. 8. Time evolved expectation value and standard deviation of particle distribution function at $x = 0$ in nonlinear Landau damping.

Table 2
Computational setup of linear two-stream instability.

t	x	N_x	m_{ion}/m_{ele}	u_{ele}	N_u	α
(0, 70]	$[0, 2\pi/k]$	128	1836	$[-5, 5]$	128	0.001
k	ξ	Polynomial	$N_z(\text{gPC})$	$N_z(\text{quad})$	Kn	cfl
0.5	$\mathcal{U}(0, 1)$	Legendre	5	9	100	0.2

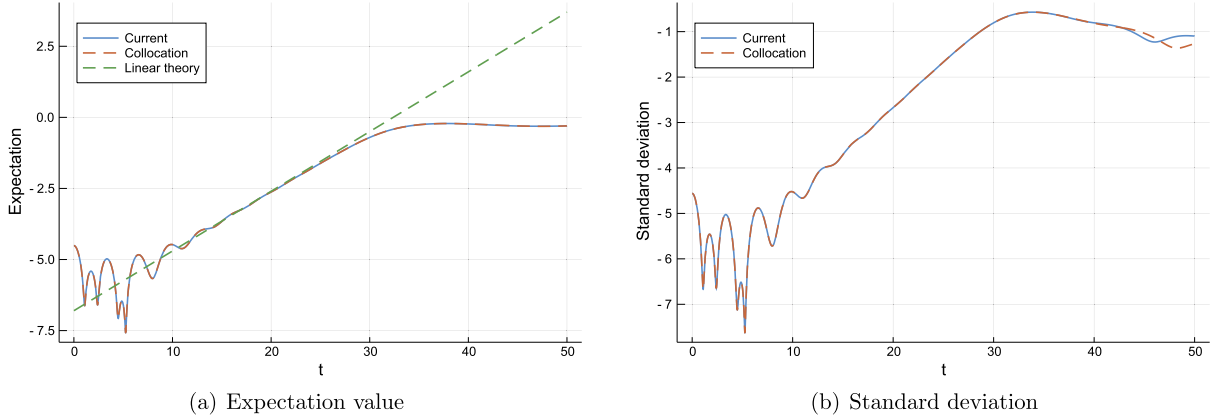


Fig. 9. Expectation value and standard deviation of electric field energy (logarithmic) in linear two-stream instability.

4.2.1. Linear case

Consider the following initial system,

$$\begin{bmatrix} n_{ion} \\ n_{ele} \\ U \\ T \\ f_{ion} \\ f_{ele} \end{bmatrix}_{t=0} = \begin{bmatrix} 1 \\ \frac{2}{7} \left[1 + \alpha \xi \left(\frac{\cos(2kx) + \cos(3kx)}{1.2} + \cos(kx) \right) \right] \\ 0 \\ 1 \\ n_{ion} \left(\frac{m_{ion}}{2\pi T} \right)^{1/2} \exp \left(-\frac{m_{ion}}{2T} (u - U)^2 \right) \\ n_{ele} \left(\frac{m_{ele}}{2\pi T} \right)^{1/2} (1 + 5u^2) \exp \left(-\frac{m_{ele}}{2T} (u - U)^2 \right) \end{bmatrix},$$

where the computational setup is listed in Table 2. Same as the Landau damping case, we fix the slow motions of ions as background, and solve the evolution of electrons.

The evolution of electric field energy is shown in Fig. 9, from which it can be seen that the numerical and theoretical solutions [1] fit well, and the uncertainties of electric energy propagate in the similar pattern as mean field. Fig. 10 provides the particle distribution function over the phase space (x, u) at $t = 70$. The swirling pattern is clearly identified in both expectation and variance values. More fine structures can be seen in the standard deviation, which provides a clearer way to quantify the stochastic evolution of particles.

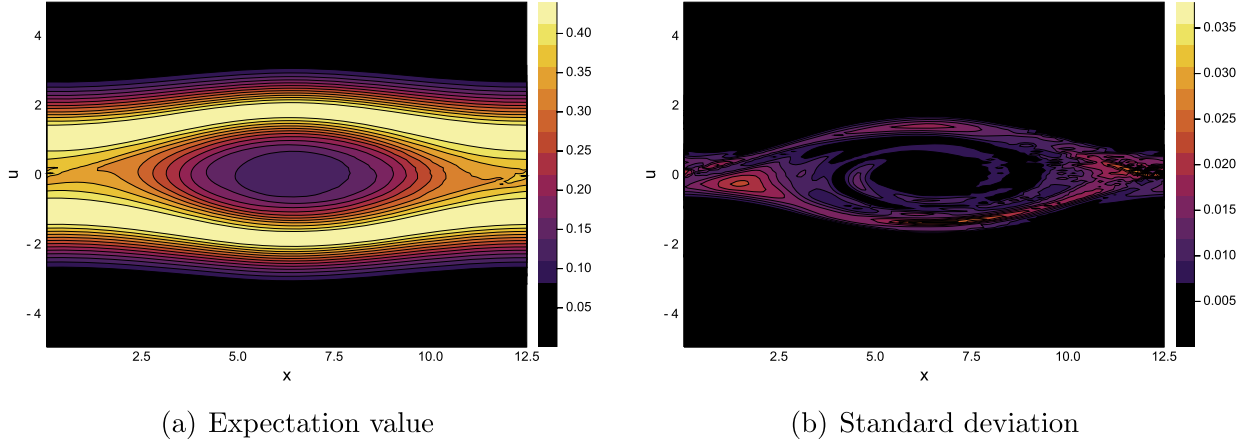


Fig. 10. Expectation value and standard deviation of particle distribution function over phase space (x, u) in linear two-stream instability.

Table 3
Computational setup of nonlinear two-stream instability.

t	x	N_x	m_{ion}/m_{ele}	u_{ele}	N_u	α
(0, 70]	$[0, 2\pi/k]$	256	1836	$[-5, 5]$	256	0.001
k	ξ	Polynomial	$N_z(gPC)$	$N_z(quad)$	Kn	cfl
0.5	$\mathcal{U}(0, 1)$	Legendre	5	9	100	0.2

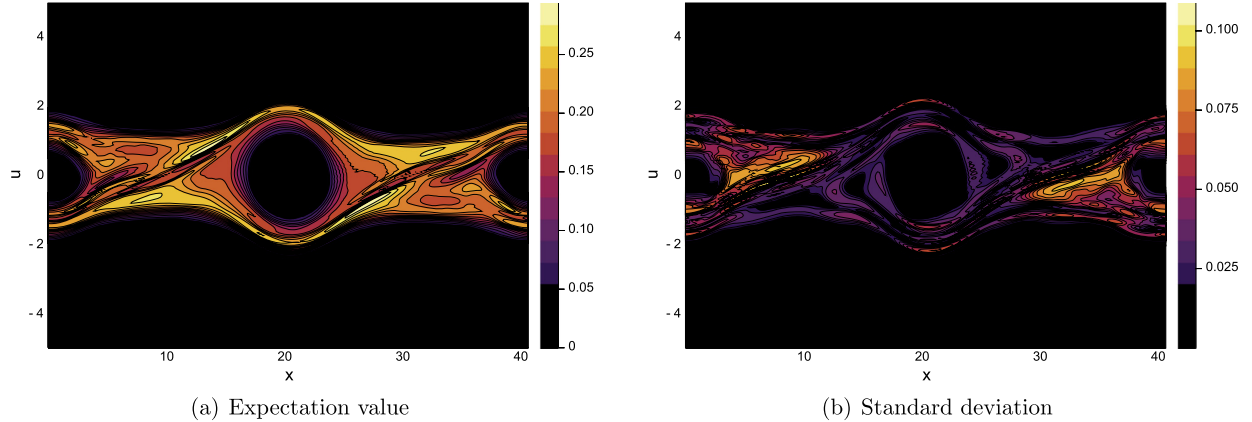


Fig. 11. Expectation value and standard deviation of particle distribution function over phase space (x, u) in nonlinear two-stream instability.

4.2.2. Nonlinear case

In the following let us consider the nonlinear case. The initial system is given as,

$$\begin{bmatrix} n_{ion} \\ n_{ele} \\ U \\ T \\ f_{ion} \\ f_{ele} \end{bmatrix}_{t=0} = \begin{bmatrix} 1 \\ \frac{1}{2} (1 + \alpha \xi * \cos(kx)) \\ 0 \\ 0.09 \\ n_{ion} \left(\frac{m_{ion}}{2\pi T}\right)^{1/2} \exp\left(-\frac{m_{ion}}{2T}(u - U)^2\right) \\ \frac{1}{2} n_{ele} \left(\frac{m_{ele}}{2\pi T}\right)^{1/2} \left(\exp\left(-\frac{m_{ele}}{2T}(u - 0.99)^2\right) + \exp\left(-\frac{m_{ele}}{2T}(u + 0.99)^2\right)\right) \end{bmatrix}.$$

The computational setups adopted here is shown in Table 3.

Fig. 11 shows the time evolution of expected particle distribution over the phase space (x, u). Due to the increasing kinetic energy from two particle streams, the particle distribution function is stretched and warped in the phase space. The pattern of standard deviation is similar as mean field, yet presenting more fine-scale structures, indicating a stronger sensitivity with respect to stochastic parameters.

Table 4
Computational setup of shear layer.

t	x	N_x	m_{ion}/m_{ele}	u_{ion}	u_{ele}	cfl
(0, 1.0]	$[-1, 1]$	100	20	$[-5, 5]$	$[-5, 5] \times \sqrt{\frac{m_{ion}}{m_{ele}}}$	0.5
ξ	Polynomial	$N_z(gPC)$	$N_z(\text{quad})$	Kn	r_g	λ_D
$\mathcal{U}(0.8, 1.2)$	Legendre	5	9	100	[0.2]	0.2

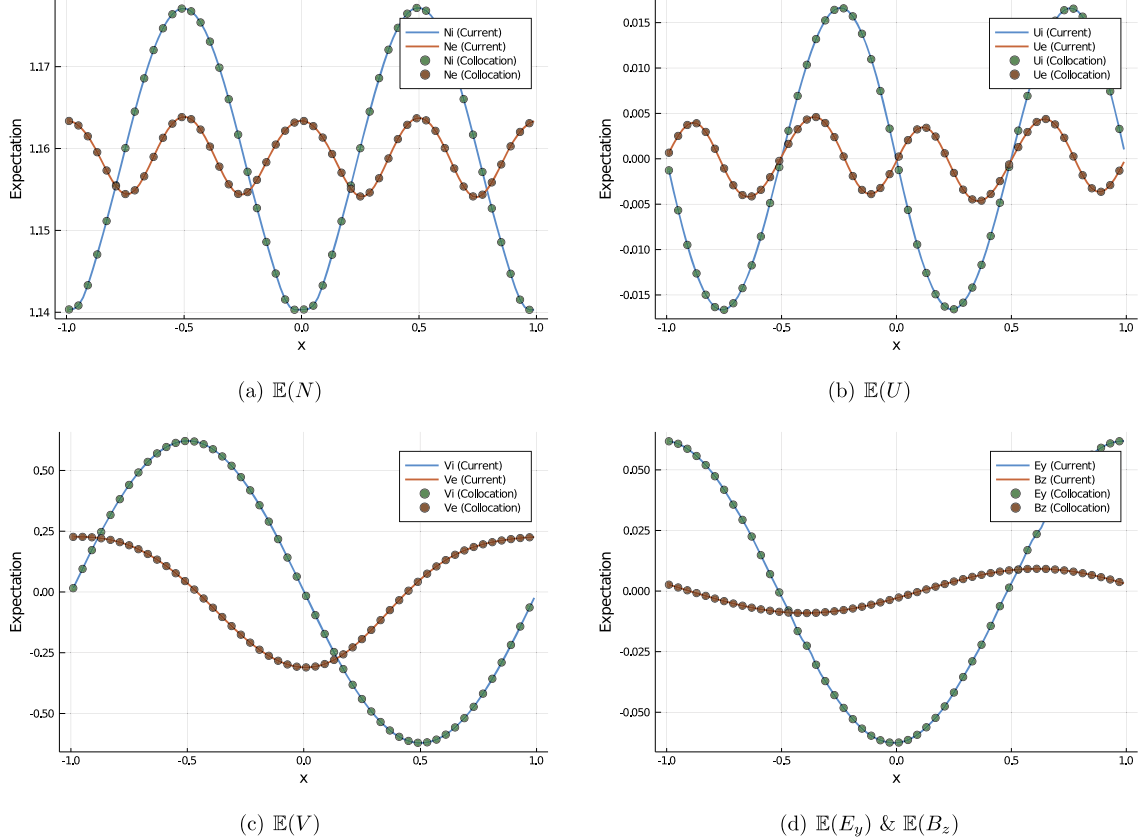


Fig. 12. Expectation values of N , U , V , E_y and B_z in shear layer at $t = 1$.

4.3. Shear layer

In the simulations of Landau damping and two-stream instability, the heavy ions with slow motions are treated as background substances. Here we append a numerical experiment of shear layer under electromagnetic fields to validate the performance of current scheme for studying multi-component plasma physics in the Vlasov limit. The initial plasma system is set as

$$\begin{bmatrix} n_{ion} \\ n_{ele} \\ U \\ V \\ W \\ T \\ E_x \\ E_y \\ E_z \\ B_x \\ B_y \\ B_z \end{bmatrix}_{t=0} = \begin{bmatrix} 1 + 0.25 |\sin(\pi x)| \\ 1 + 0.25 |\sin(\pi x)| \\ 0 \\ -\xi \sin(\pi x) \\ 0 \\ 1 \\ 0 \\ 0 \\ 0 \\ 0 \\ 0 \\ 0.01 \sin(\pi x) \end{bmatrix}.$$

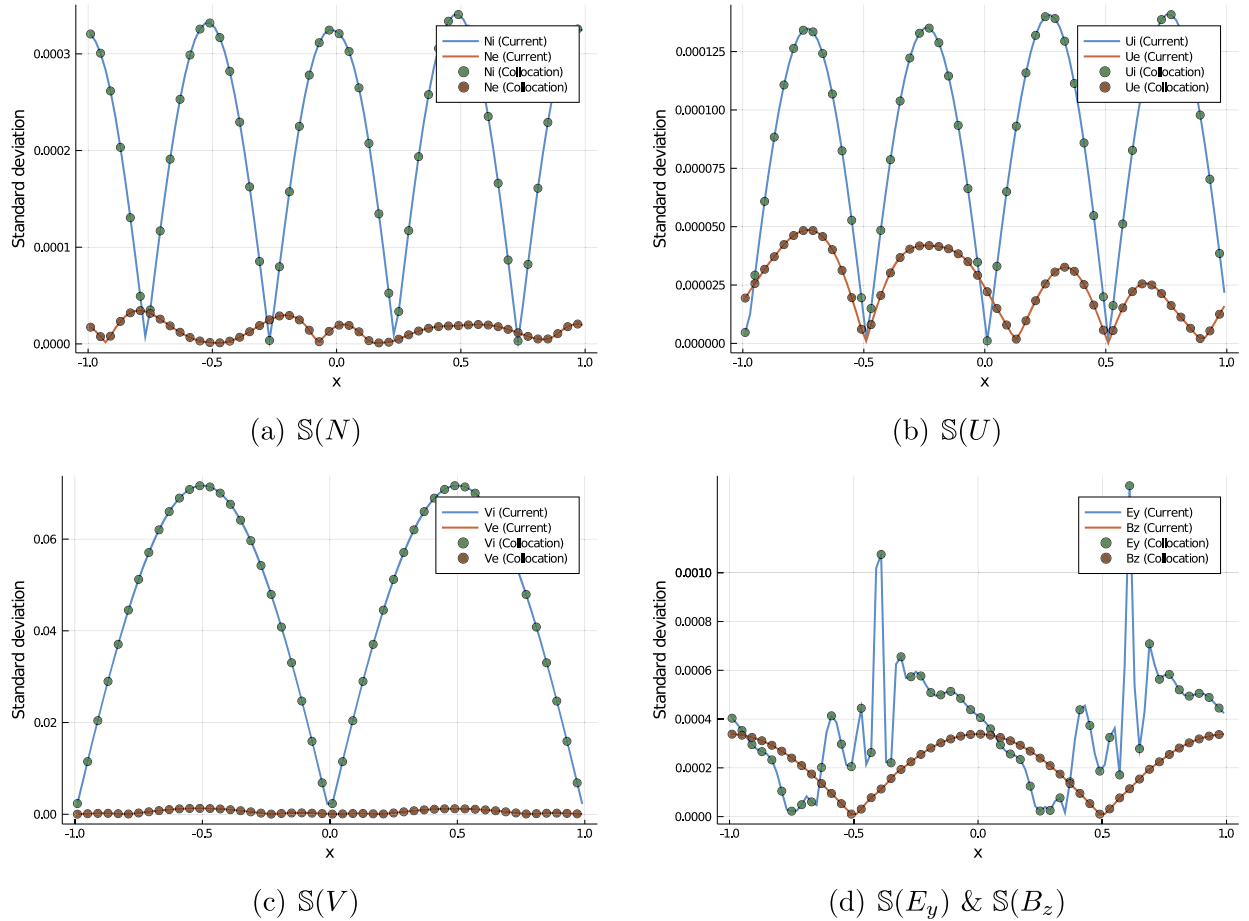


Fig. 13. Standard deviations of N , U , V , E_y and B_z in shear layer at $t = 1$.

The computational setup is provided in Table 4.

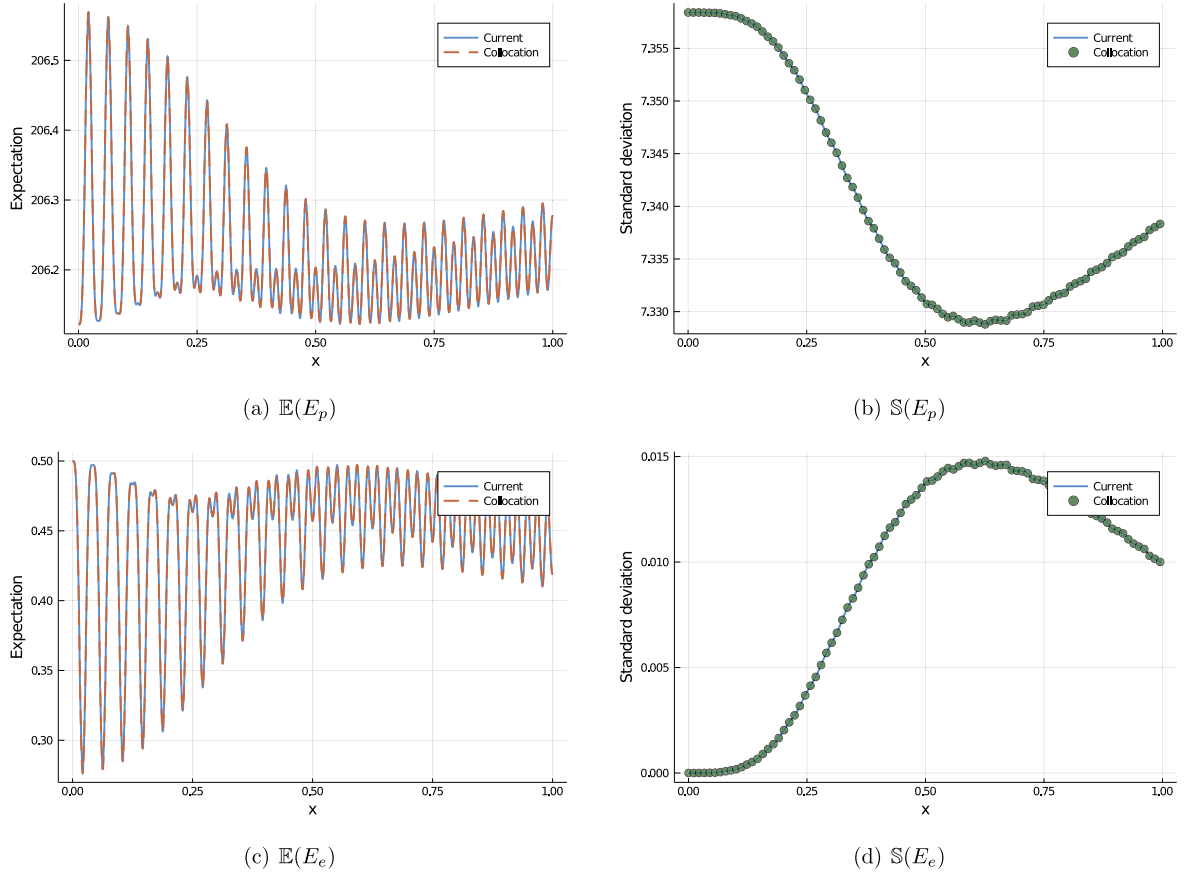
Fig. 12 and 13 present the expected profiles of macroscopic variables and their standard deviations inside the domain. The reference solutions are produced by the gas-kinetic scheme [36] with standard collocation setting. As is shown, the current scheme provides equivalent solutions as benchmark. In the collisionless Vlasov regime, the transports of ions and particles are being loosely coupled, leading to different wave frequencies of substances. Fig. 14 shows the time trajectories of total energy of plasma and electromagnetic field throughout the domain. With the essential plasma oscillations, similar energy evolution modes as the two-stream instability emerge. The modifications of traveling pattern can be observed in both plasma and electromagnetic energies, which clearly demonstrates the coupling and transformation between particle and fields.

Besides, as illustrated in Sec. 3.4, the pseudo setting of speed of light is used in the simulations. In order to analyze its effects on the numerical solutions, we conduct a numerical experiment for this shear layer problem under different speed of light. The computational setups are adopted the same way in Table 4 and corresponding results are shown in Fig. 15. As can be seen, with the speed of light varies from 80 to 150, the relative variations of solutions are below 2.5%, which validates the current treatment of numerical speed of light.

4.4. Brio-Wu shock tube

After the validation of current scheme in the Vlasov limit, let us turn to another limiting regime, i.e. the magnetohydrodynamic (MHD) transport problem under continuum assumption. In this case, we employ the Brio-Wu shock tube [7] as benchmark case for ideal MHD solutions.

In the simulation, the initial background of deterministic solutions is consistent with the Sod problem, with an additional magnetic discontinuity, i.e.,

Fig. 14. Standard deviations of N , U , V , E_y and B_z in shear layer at $t = 1$.

$$\begin{bmatrix} n_{ion} \\ n_{ele} \\ U \\ p \\ E_x \\ E_y \\ E_z \\ B_x \\ B_y \\ B_z \\ \phi \\ \psi \end{bmatrix}_L = \begin{bmatrix} 1 \\ 1 \\ 0 \\ 1 \\ 0 \\ 0 \\ 0 \\ 0.75 \\ 1 \\ 0 \\ 0 \\ 0 \end{bmatrix},$$

for the left half, and

$$\begin{bmatrix} n_{ion} \\ n_{ele} \\ U \\ p \\ E_x \\ E_y \\ E_z \\ B_x \\ B_y \\ B_z \\ \phi \\ \psi \end{bmatrix}_R = \begin{bmatrix} 0.125 \\ 0.125 \\ 0 \\ 0.8 \\ 0 \\ 0 \\ 0 \\ 0.75 \\ -1 \\ 0 \\ 0 \\ 0 \end{bmatrix},$$

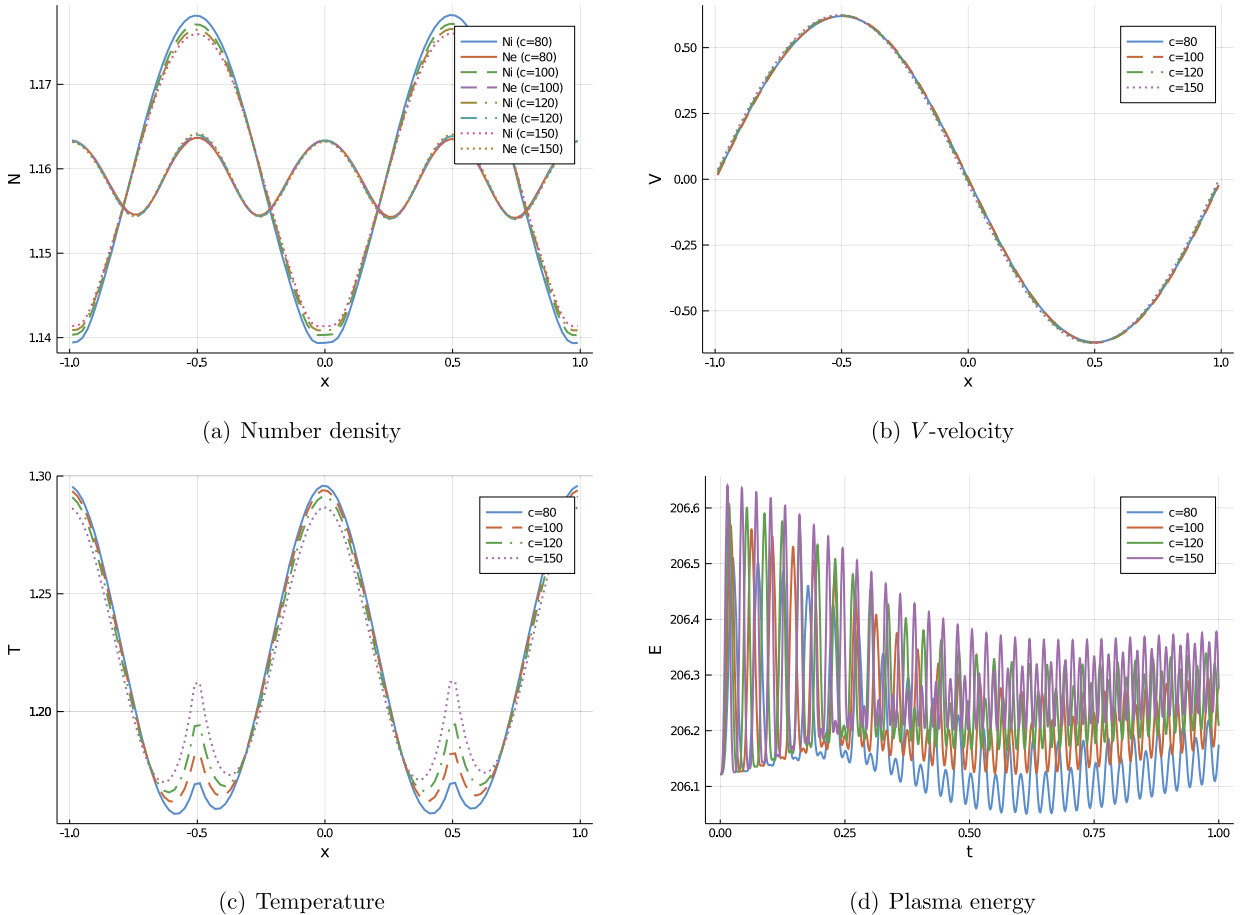


Fig. 15. Profiles of number density, V -velocity, temperature and plasma energy in shear layer at different settings of speed of light.

Table 5
Computational setup of Brio-Wu shock tube.

t	x	N_x	m_{ion}/m_{ele}	u_{ion}	u_{ele}	cfl
(0, 0.1]	[0, 1]	400	1836	[-5, 5]	$[-5, 5] \times \sqrt{\frac{m_{ion}}{m_{ele}}}$	0.3
ξ	Polynomial	$N_z(gPC)$	$N_z(quad)$	Kn	r_g	λ_D
$\mathcal{U}(0.95, 1.05)$	Legendre	5	9	1.0×10^{-6}	[0.003, 100]	0.01

for the right half. The computational setup is listed in Table 5. To recover the ideal MHD solutions, here the interspecies coefficients v_{ie} is set as zero.

4.4.1. Case 1: stochastic flow field

First, we consider the uncertainties of plasma density in the left half tube, with $n_{ion,L} = n_{ele,L} = \xi$. The numerical expected solutions of macroscopic variables under different reference gyroradius at $t = 0.1$ are shown in Fig. 16. It is known that the evolution of flow and electromagnetic fields can be well described by MHD equations when r_g is small. At $r_g = 0.003$, besides the typical wave structures in the classic Sod problem, a compound wave emerges around the tube center. As illustrated by Brio and Wu [7], with the nonconvexity of ideal MHD equation, this wave structure is induced from initial magnetic discontinuity. From Fig. 16(a)-(c), we see clearly that the current kinetic solution approaches the MHD one, and presents similar shape and location of slow compound wave. It identifies the asymptotic preserving (AP) property of the current scheme. As analyzed in [42], the steeper edges of the structure corresponds to the slow shock component of the slow compound wave. The position of a well-formed slow shock is slightly different from the MHD shock [39].

As the gyroradius r_g increases, the electric and Lorentz force decreases accordingly. The effects of charge separation are enhanced, and the omitted terms, e.g. the Hall current term, become important. The plasma gradually manifests itself as dielectric material. As a result, the magnetic diffusion is enhanced, and the wave structures from discontinuous magnetic field B_y are flattened. When $r_g = 100$, at this point the gyroradius is much larger than the characteristic length of the

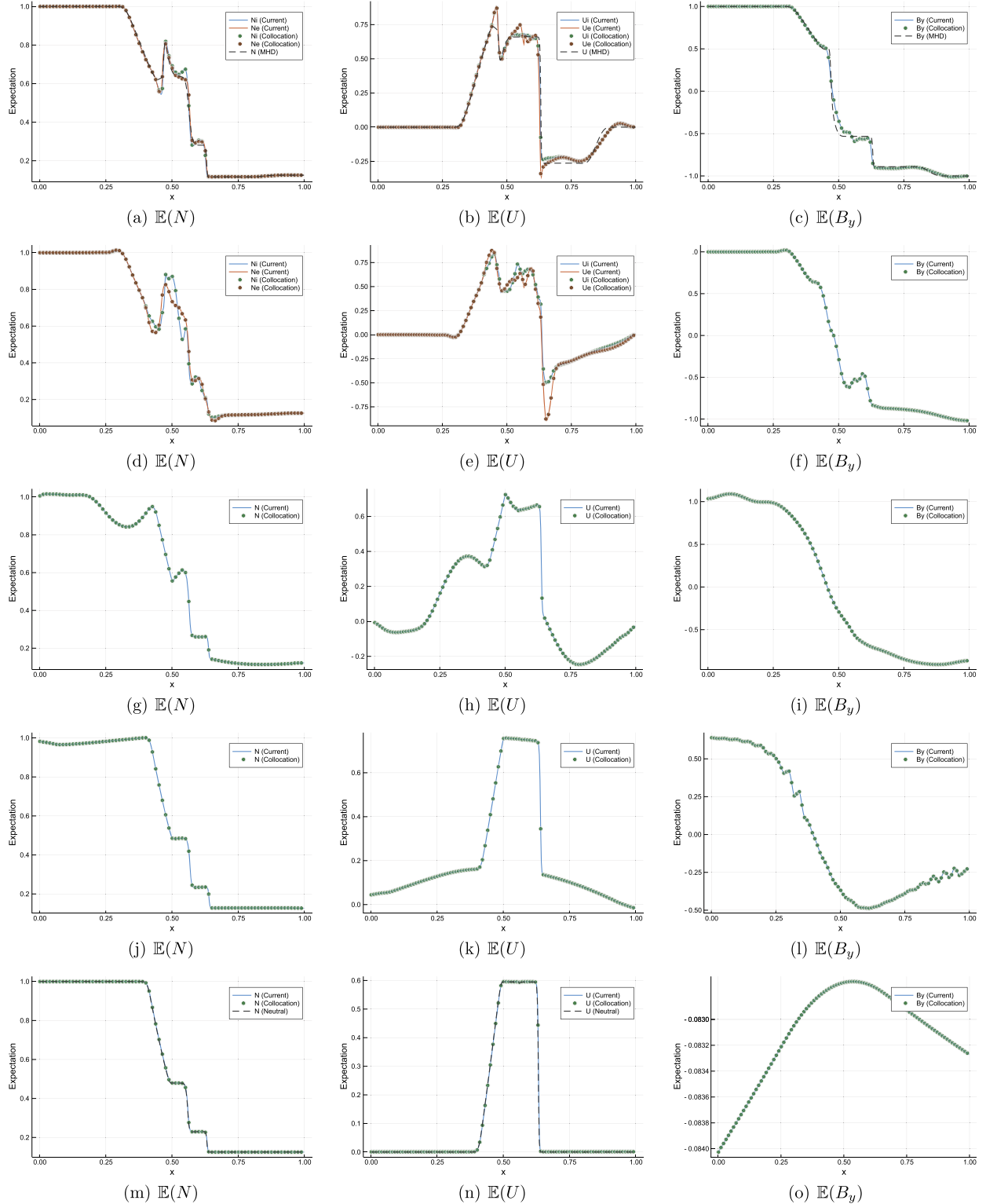


Fig. 16. Expectation values of N , U and B_y in Brio-Wu shock tube with density uncertainty at $t = 0.1$ (row 1: $r_g = 0.003$, row 2: $r_g = 0.01$, row 3: $r_g = 0.1$, row 4: $r_g = 1$, row 5: $r_g = 100$).

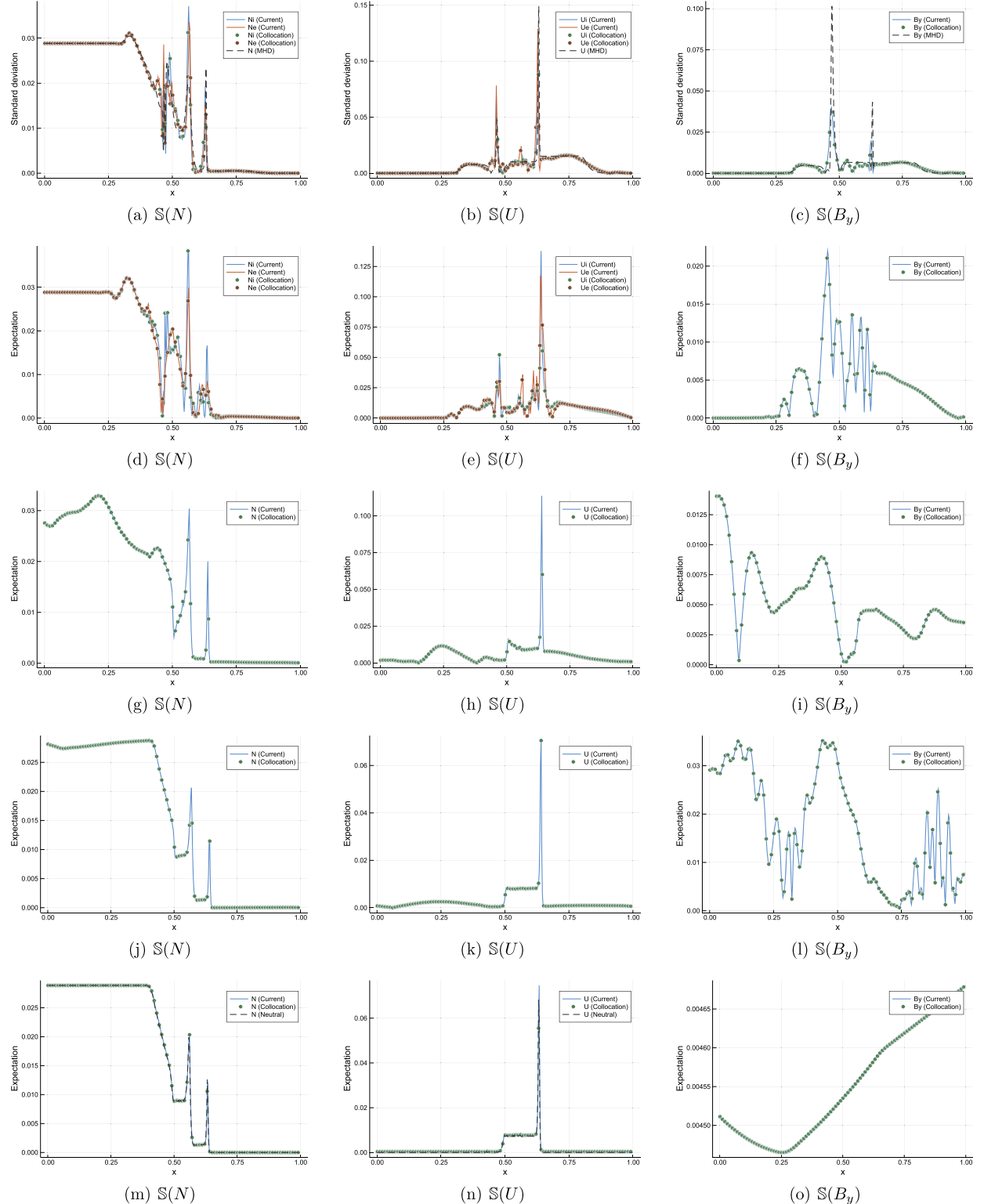


Fig. 17. Standard deviations of N , U and B_y in Brio-Wu shock tube with density uncertainty at $t = 0.1$ (row 1: $r_g = 0.003$, row 2: $r_g = 0.01$, row 3: $r_g = 0.1$, row 4: $r_g = 1$, row 5: $r_g = 100$).

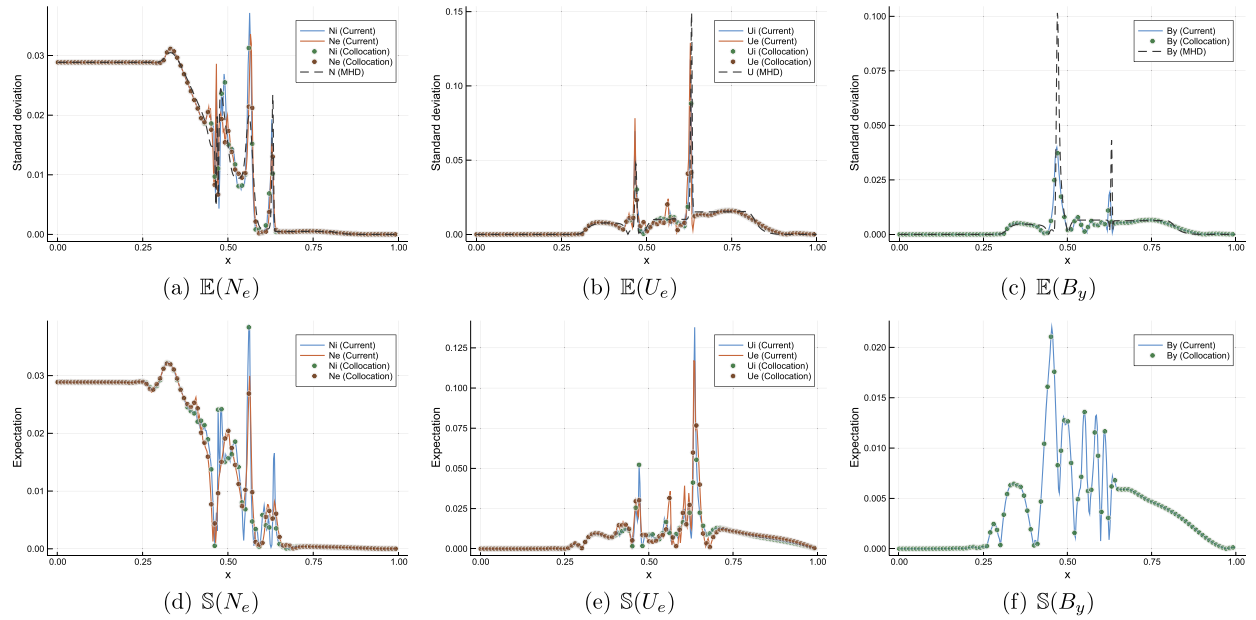


Fig. 18. Expectations and standard deviations of N_e , U_e and B_y in Brio-Wu shock tube with density uncertainty at $t = 0.1$ at different mesh resolution.

shock tube, and thus plasma behaves as neutral gas, and the Brio-Wu shock tube degenerates into a standard Sod case. In Fig. 16(m) and (n), we see the current scheme provides equivalent solutions as Euler equations, indicating the AP property of the current scheme in the Euler limit.

Fig. 17 presents the standard deviations at the same output instant. Generally, the uncertainties travel along with the wave structure of expectation values and present similar propagating patterns. Typical wave structures serve as sources of local maximums of variance. Compared with the expected value, its variance is more sensitive to physical discontinuities and holds finer-scale structures due to the spectrum formulation in the random space. As a result, the overshoots near contact discontinuity and shock emerge, and the steeper edges lead to some high-frequency variances around the central compound wave. To further verify this result is not due to numerical error, we conduct a grid-converged experiment. The expectations and standard deviations of electron density, velocity and magnetic field B_y in a refining series are shown in Fig. 18, which clearly shows the grid independency of this phenomenon.

Fig. 19 presents the expectations and standard deviations of particle distribution function at different reference gyroradii. As is shown, the discontinuities in macroscopic expectations and overshoots in standard deviations come from the uncertainties contained in the particle distribution function near the center of velocity space. From MHD to Euler regimes, the randomness on particles get reduced and smoothed, resulting in gentle profiles of macroscopic quantities.

4.4.2. Case 2: stochastic magnetic field

In the second case, we turn to the uncertainties from magnetic field in the left half tube, with $B_{y,L} = \xi$. The numerical solutions of macroscopic variables under different reference gyroradius at $t = 0.1$ are shown in Fig. 20 and 21. For the expected values in Fig. 20, we see that different initial stochastic conditions don't significantly change the wave structures of mean field. Both MHD and Euler limits are precisely preserved under stochastic magnetic field.

Fig. 21 presents the corresponding standard deviations of macroscopic system. As can be seen, the uncertainties manifest the consistent propagating patterns of expected values. Different from the previous case, here the high-frequency variance of density in compound wave region is much reduced, which indicates this phenomenon comes from the uncertain densities. As r_g increases, the wave structures around tube center becomes even more complicated in the transition regime $r_g = 0.01$, and simplify again when it comes to $r_g = 0.1$, which demonstrates the complex nonlinearity from Hall current, two-fluid effects, etc. The increasing gyroradius doesn't lead to a simple process of monotonic variation.

This test case clearly shows the consistency and distinction of propagation modes between expectation value and variance. It also illustrates the capacity of current scheme to simulate multi-scale and multi-physics plasma transports, and capture the propagation of uncertainties in different regimes.

5. Conclusion

Plasma dynamics is associated with an intrinsic multi-scale nature due to the large variations of particle density and temperature, as well as the characteristic scales of the local structures. Based on the multi-component BGK model and Maxwell's equations, a stochastic kinetic scheme (see Table 6 for nomenclature) with hybrid Galerkin-collocation strat-

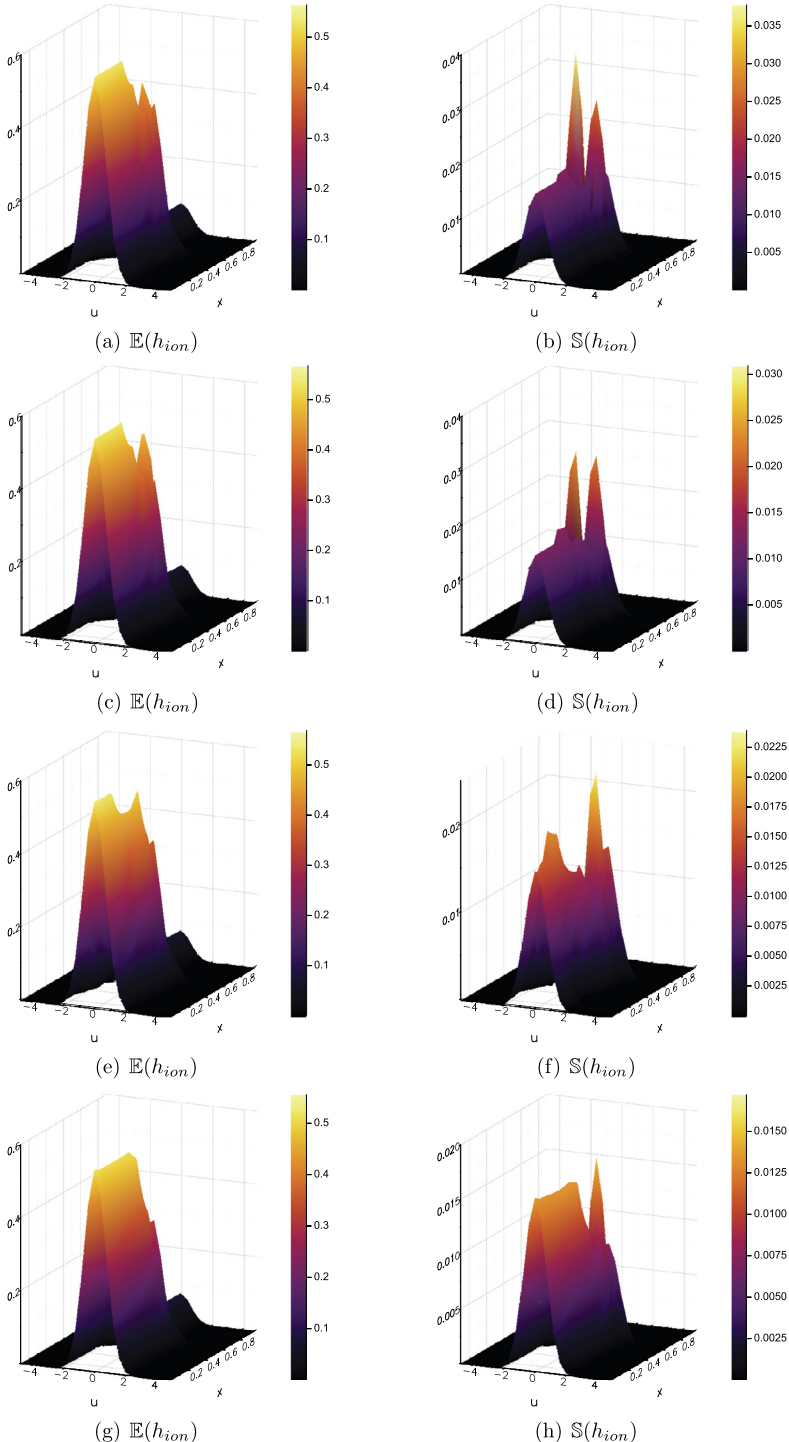


Fig. 19. Expectations and variances of reduced ion distribution h_{ion} , in Brio-Wu shock tube with density uncertainty at $t = 0.1$ (row 1: $r_g = 0.003$, row 2: $r_g = 0.01$, row 3: $r_g = 0.1$, row 4: $r_g = 1$).

egy has been constructed in this paper, which allows for a unified numerical simulation for multi-scale plasma physics. Based on the cross-scale modeling, the solution algorithm is able to capture both equilibrium magnetohydrodynamics and non-equilibrium gyrations of charged particles simultaneously, and recover the scale-dependent plasma physics along with the emergence, propagation, and evolution of randomness. The asymptotic-preserving property of the scheme is validated through theoretical analysis and numerical tests.

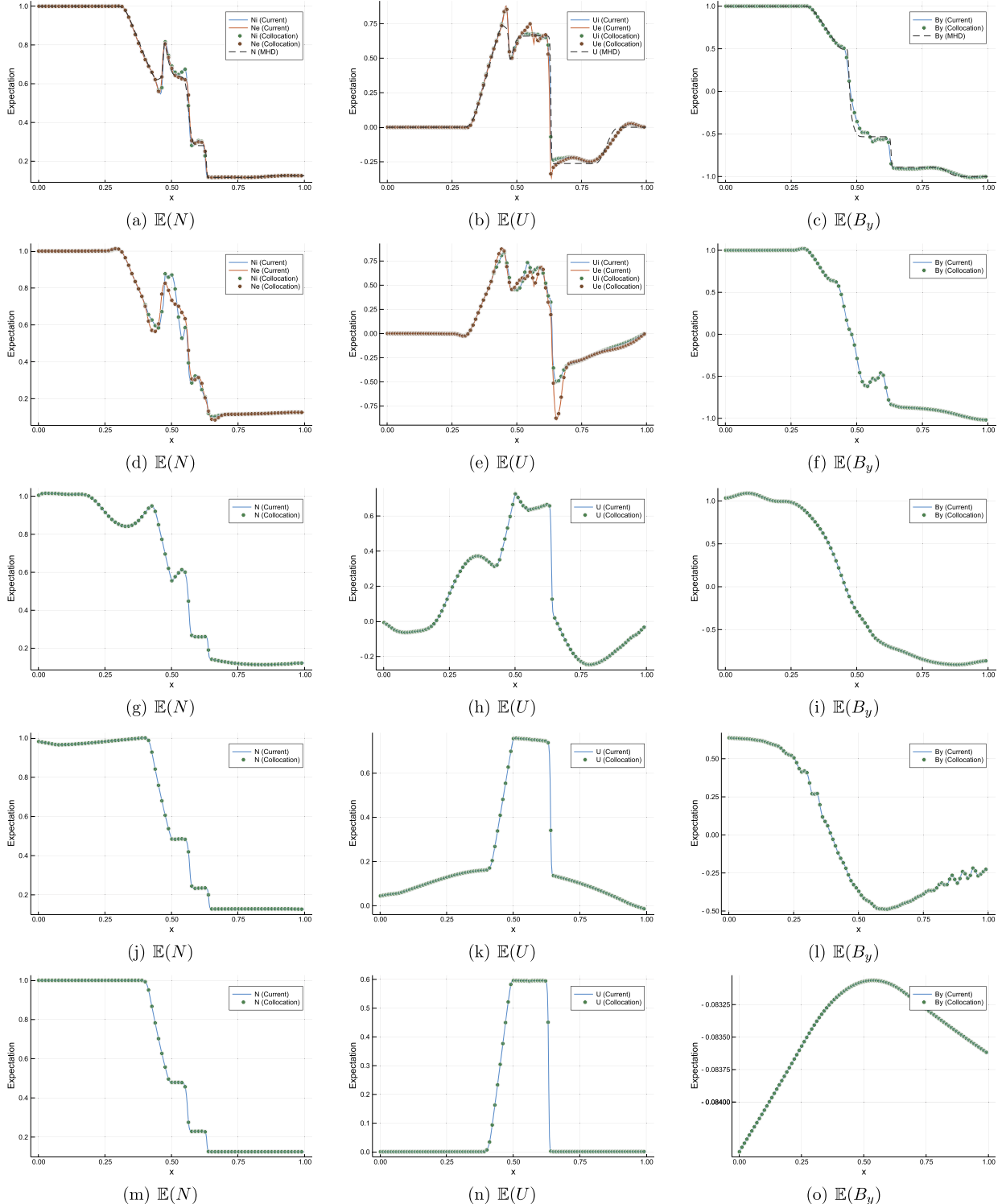


Fig. 20. Expectation values of N , U and B_y in Brio-Wu shock tube with magnetic uncertainty at $t = 0.1$ (row 1: $r_g = 0.003$, row 2: $r_g = 0.01$, row 3: $r_g = 0.1$, row 4: $r_g = 1$, row 5: $r_g = 100$).

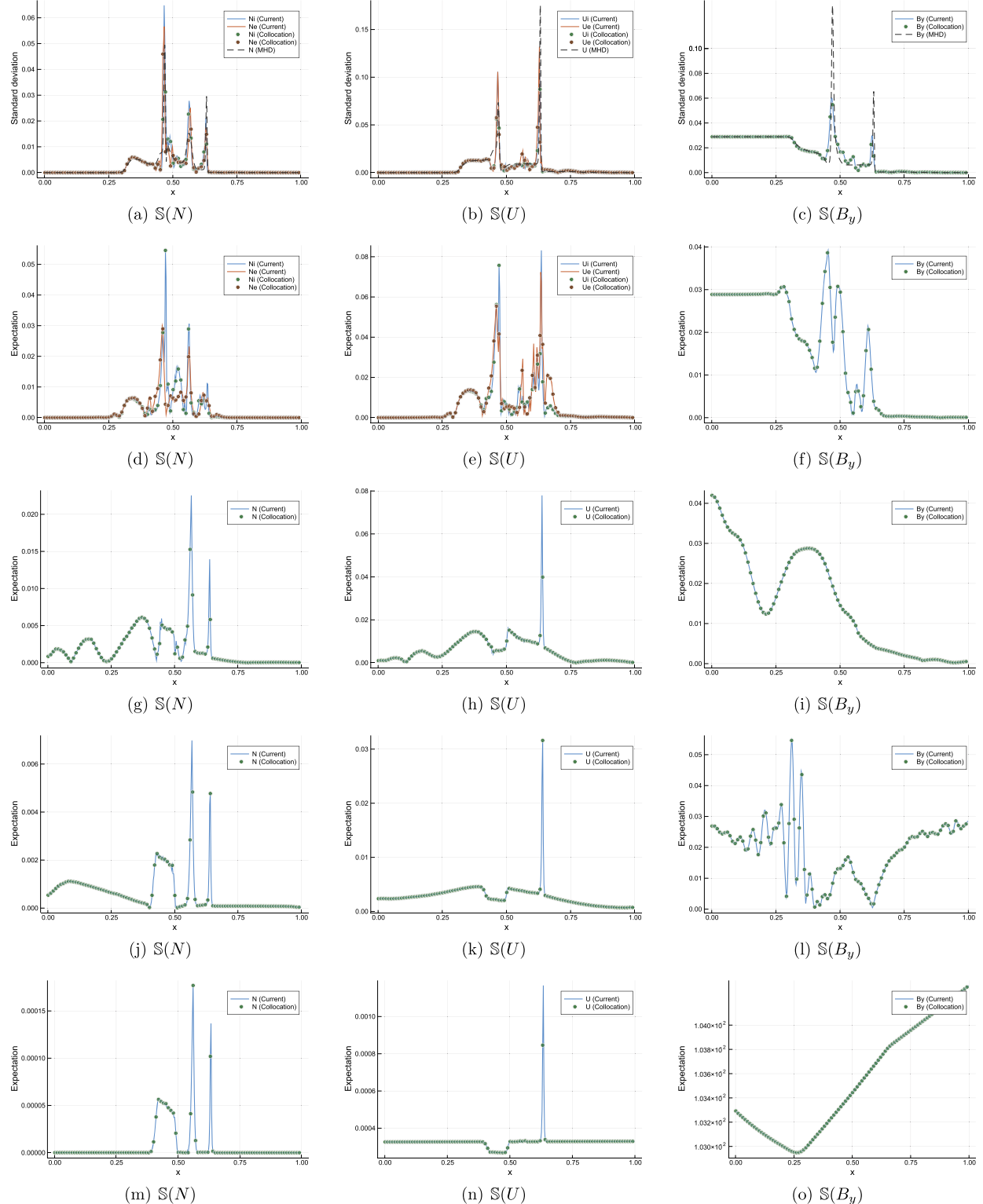


Fig. 21. Standard deviations of N , U and B_y in Brio-Wu shock tube with magnetic uncertainty at $t = 0.1$ (row 1: $r_g = 0.003$, row 2: $r_g = 0.01$, row 3: $r_g = 0.1$, row 4: $r_g = 1$, row 5: $r_g = 100$).

Table 6

Nomenclature of stochastic kinetic scheme.

k_B	Boltzmann constant
ε_0	vacuum permittivity
μ_0	vacuum permeability
e	elementary charge
c	speed of light
q_α	charge of species α , with $q_\alpha = \pm e$ ($\alpha = \text{ion, ele}$)
m_α	particle mass of species α
n_α	number density of species α
ρ_α	density of species α
\mathbf{U}_α	macroscopic velocity of species α
T_α	temperature of species α
\mathbf{P}_α	stress tensor of species α
p_α	pressure of species α
\mathbf{q}_α	heat flux of species α
\mathbf{W}_α	macroscopic conservative variables of species α (density, momentum, energy)
f_α	particle distribution function of species α
\mathbf{u}	particle velocity
\mathbf{a}_α	electromagnetic force acting on species α
Q_α	kinetic collision operator of species α
\mathcal{M}_α	equilibrium distribution function of species α
\mathbf{E}	electric field
\mathbf{B}	magnetic field
ϕ	correction potential for \mathbf{E} in perfectly hyperbolic Maxwell's equations
ψ	correction potential for \mathbf{B} in perfectly hyperbolic Maxwell's equations
σ	charge density
\mathbf{J}	current density
\mathbf{M}	abbreviation of electromagnetic variables ($\mathbf{E}, \mathbf{B}, \phi, \psi$)
ϖ	vector of collision invariants
ν_α	collision frequency of species α
ν_{ie}	interaction frequency between ion and electron
τ_α	Collision time of species α with $\tau_\alpha = 1/\nu_\alpha$
\mathbf{F}_α^W	flux for macroscopic conservative variables of species α
\mathbf{F}_α^f	flux for particle distribution function of species α
\mathbf{F}^M	flux for electromagnetic variables
L_N	generalized polynomial chaos expansion of any stochastic variable L with degree N
$\hat{\mathbf{i}}$	vector of generalized polynomial chaos coefficients of any stochastic variable L
Φ	orthogonal polynomials in random space \mathbf{z}
ϱ	probability density function of random variable \mathbf{z}
Kn	Knudsen number
r_L	gyroradius
λ_D	Debye length
$H[x]$	Heaviside step function

CRediT authorship contribution statement

Tianbai Xiao: Conceptualization, Formal analysis, Investigation, Methodology, Project administration, Software, Visualization, Writing – original draft, Writing – review & editing. **Martin Frank:** Conceptualization, Formal analysis, Methodology, Project administration, Resources, Supervision, Writing – original draft, Writing – review & editing.

Declaration of competing interest

The authors declare that there is no conflict of interest to this work. The authors declare that they have no known competing financial interests or personal relationships that could have appeared to influence the work reported in this paper.

Acknowledgement

The current research is funded by the Alexander von Humboldt Foundation (Ref3.5-CHN-1210132-HFST-P).

References

- [1] Francis F. Chen, Introduction to Plasma Physics, Springer Science & Business Media, 2012.
- [2] National Research Council, Plasma Science Committee, Plasma 2010 Committee, et al., Plasma Science: Advancing Knowledge in the National Interest, vol. 3, National Academies Press, 2008.
- [3] Vahid Vahedi, Maheswaran Surendra, A Monte Carlo collision model for the particle-in-cell method: applications to argon and oxygen discharges, Comput. Phys. Commun. 87 (1–2) (1995) 179–198.

- [4] Francis Filbet, Eric Sonnendrücker, Pierre Bertrand, Conservative numerical schemes for the Vlasov equation, *J. Comput. Phys.* 172 (1) (2001) 166–187.
- [5] Nicolas Crouseilles, Thomas Respaud, Eric Sonnendrücker, A forward semi-Lagrangian method for the numerical solution of the Vlasov equation, *Comput. Phys. Commun.* 180 (10) (2009) 1730–1745.
- [6] Jing-Mei Qiu, Andrew Christlieb, A conservative high order semi-Lagrangian WENO method for the Vlasov equation, *J. Comput. Phys.* 229 (4) (2010) 1130–1149.
- [7] Moysey Brio, Cheng Chin Wu, An upwind differencing scheme for the equations of ideal magnetohydrodynamics, *J. Comput. Phys.* 75 (2) (1988) 400–422.
- [8] Kenneth G. Powell, Philip L. Roe, Timur J. Linde, Tamas I. Gombosi, Darren L. De Zeeuw, A solution-adaptive upwind scheme for ideal magnetohydrodynamics, *J. Comput. Phys.* 154 (2) (1999) 284–309.
- [9] Pierre Degond, Fabrice Deluzet, Laurent Navoret, An-Bang Sun, Marie-Hélène Vignal, Asymptotic-preserving particle-in-cell method for the Vlasov-Poisson system near quasineutrality, *J. Comput. Phys.* 229 (16) (2010) 5630–5652.
- [10] Pierre Degond, Fabrice Deluzet, Asymptotic-preserving methods and multiscale models for plasma physics, *J. Comput. Phys.* 336 (2017) 429–457.
- [11] Carlo Cercignani, *The Boltzmann Equation and Its Applications*, Springer, 1988.
- [12] National Institute of Standards and Technology, *The NIST Reference on Constants, Units, and Uncertainty*, May 2019.
- [13] Dongbin Xiu, *Numerical Methods for Stochastic Computations: A Spectral Method Approach*, Princeton University Press, 2010.
- [14] Claudio Canuto, Alfio Quarteroni, Approximation results for orthogonal polynomials in Sobolev spaces, *Math. Comput.* 38 (157) (1982) 67–86.
- [15] Dongbin Xiu, Jan S. Hesthaven, High-order collocation methods for differential equations with random inputs, *SIAM J. Sci. Comput.* 27 (3) (2005) 1118–1139.
- [16] Jingwei Hu, Shi Jin, Ruiwen Shu, A stochastic Galerkin method for the Fokker–Planck–Landau equation with random uncertainties, in: XVI International Conference on Hyperbolic Problems: Theory, Numerics, Applications, Springer, 2016, pp. 1–19.
- [17] Shi Jin, Yuhua Zhu, Hypocoercivity and uniform regularity for the Vlasov–Poisson–Fokker–Planck system with uncertainty and multiple scales, *SIAM J. Math. Anal.* 50 (2) (2018) 1790–1816.
- [18] Zhiyan Ding, Shi Jin, Random regularity of a nonlinear Landau Damping solution for the Vlasov–Poisson equations with random inputs, *Int. J. Uncertain. Quantificat.* 9 (2) (2019).
- [19] Edward G. Phillips, Howard C. Elman, A stochastic approach to uncertainty in the equations of MHD kinematics, *J. Comput. Phys.* 284 (2015) 334–350.
- [20] Kazuo Yamazaki, Stochastic Hall-magneto-hydrodynamics system in three and two and a half dimensions, *J. Stat. Phys.* 166 (2) (2017) 368–397.
- [21] Jingwei Hu, Shi Jin, Uncertainty quantification for kinetic equations, in: *Uncertainty Quantification for Hyperbolic and Kinetic Equations*, Springer, 2017, pp. 193–229.
- [22] Liu Liu, Shi Jin, Hypocoercivity based sensitivity analysis and spectral convergence of the stochastic Galerkin approximation to collisional kinetic equations with multiple scales and random inputs, *Multiscale Model. Simul.* 16 (3) (2018) 1085–1114.
- [23] Tianbai Xiao, Martin Frank, A stochastic kinetic scheme for multi-scale flow transport with uncertainty quantification, arXiv preprint, arXiv:2002.00277, 2020.
- [24] Clément Mouhot, Lorenzo Pareschi, Fast algorithms for computing the Boltzmann collision operator, *Math. Comput.* 75 (256) (2006) 1833–1852.
- [25] Lei Wu, Jun Zhang, Jason M. Reese, Yonghao Zhang, A fast spectral method for the Boltzmann equation for monatomic gas mixtures, *J. Comput. Phys.* 298 (2015) 602–621.
- [26] Tianbai Xiao, Kun Xu, Qingdong Cai, A unified gas-kinetic scheme for multiscale and multicomponent flow transport, *Appl. Math. Mech.* (2019) 1–18.
- [27] Pierre Andries, Kazuo Aoki, Benoit Perthame, A consistent BGK-type model for gas mixtures, *J. Stat. Phys.* 106 (5) (2002) 993–1018.
- [28] T.F. Morse, Energy and momentum exchange between nonequipartition gases, *Phys. Fluids* 6 (10) (1963) 1420–1427.
- [29] Sha Liu, Yihua Liang, Asymptotic-preserving Boltzmann model equations for binary gas mixture, *Phys. Rev. E* 93 (2) (2016) 023102.
- [30] S.I. Braginskii, Transport processes in a plasma, *Rev. Plasma Phys.* 1 (1965).
- [31] C-D. Munz, Pascal Omnes, Rudolf Schneider, Eric Sonnendrücker, Ursula Voss, Divergence correction techniques for Maxwell solvers based on a hyperbolic model, *J. Comput. Phys.* 161 (2) (2000) 484–511.
- [32] Nicolas Crouseilles, Shi Jin, Liu Liu, Mohammed Lemou, Nonlinear geometric optics based multiscale stochastic Galerkin methods for highly oscillatory transport equations with random inputs, *Math. Model. Numer. Anal.* 54 (6) (2021) 1849–1882.
- [33] Mikhail N. Kogan, *Rarefied Gas Dynamics*, Plenum Press, 1969.
- [34] Kun Xu, Juan-Chen Huang, A unified gas-kinetic scheme for continuum and rarefied flows, *J. Comput. Phys.* 229 (20) (2010) 7747–7764.
- [35] Tianbai Xiao, Qingdong Cai, Kun Xu, A well-balanced unified gas-kinetic scheme for multiscale flow transport under gravitational field, *J. Comput. Phys.* 332 (2017) 475–491.
- [36] Chang Liu, Kun Xu, A unified gas kinetic scheme for continuum and rarefied flows V: multiscale and multi-component plasma transport, *Commun. Comput. Phys.* 22 (5) (2017) 1175–1223.
- [37] Tianbai Xiao, Chang Liu, Kun Xu, Qingdong Cai, A velocity-space adaptive unified gas kinetic scheme for continuum and rarefied flows, *J. Comput. Phys.* (2020) 109535.
- [38] Kun Xu, *Direct Modeling for Computational Fluid Dynamics: Construction and Application of Unified Gas-Kinetic Schemes*, World Scientific, 2015.
- [39] Ammar Hakim, John Loverich, Uri Shumlak, A high resolution wave propagation scheme for ideal two-fluid plasma equations, *J. Comput. Phys.* 219 (1) (2006) 418–442.
- [40] Lawrence F. Shampine, Implementation of Rosenbrock methods, *ACM Trans. Math. Softw.* 8 (2) (1982) 93–113.
- [41] L. Landau, On the vibration of the electronic plasma, *J. Phys.* 10 (1) (1946) 25–34.
- [42] Uri Shumlak, J. Loverich, Approximate Riemann solver for the two-fluid plasma model, *J. Comput. Phys.* 187 (2) (2003) 620–638.